Mechanisms of Environmentally Induced Crack Initiation in Humid Air for New-Generation Al-Zn-Mg-Cu Alloys

CORROSION
The Journal of Science and Engineering

Mechanisms of environmentally induced crack initiation in humid air in new generation Al-Zn-Mg-Cu alloys

Journal:	*CORROSION*
Manuscript ID	CJ-2304-OA-4336.R1
Manuscript Type:	Original Article
Date Submitted by the Author:	n/a
Complete List of Authors:	Burnett, Timothy Laurence; The University of Manchester, Materials Euesden, Ryan; The University of Manchester Grant, Cameron; The University of Manchester Curd, Matthew; The University of Manchester Garner, Alistair; Jacobs Engineering Group Inc Aboura, Yasser; TWI Yao, Yichao; The University of Manchester Barrett, Zak; Airbus Engel, Christian; Airbus Holroyd, N J Henry ; Home, Prangnell, Philip; The University of Manchester
Key Words:	hydrogen embrittlement, stress corrosion cracking, aluminum alloy, environmentally assisted corrosion, aerospace

Mechanisms of environmentally induced crack initiation in humid air in new generation Al-Zn-Mg-Cu alloys

Tim L. Burnett, Ryan Euesden, Yasser Aboura, Yichao Yao, Matthew E. Curd, Cameron Grant, Al Garner, N. J. Henry Holroyd, Zak Barrett, Christian E. Engel and Phil B. Prangnell

Abstract

Recent experience has shown that new-generation 7xxx-series alloys, that have a high Zn content and Zn/Mg ratios, have a greater susceptibility to Hydrogen-Environmental Induced Cracking (H-EIC) on exposure to humid air than more established materials, like AA7050. In this study we report new evidence of the EIC initiation and crack growth behaviour of two new generation alloys, AA7085 and AA7449, when exposed to 50% humidity. In-situ, time lapse, optical imaging over large areas has enabled the exact initiation sites to be identified and investigated with high-resolution fractographic studies, providing evidence for the sequence and mechanisms of initiation and transition to sustained cracking. A consistent behaviour was observed for both alloys. This has revealed that only minute-scale corrosion reactions, involving highly localised condensed water, are necessary for initiation. The preferred initiation sites are metal ligaments between surface-connected pore-clusters and/or intermetallic particles that are subjected to high stress concentration and undergo mechanical damage with associated higher levels of local oxidation. The growth of short proto-cracks from these sites is a distinct stage and displays intermittent arrest markings evidenced by localised corrosion. In contrast, in humid air environments, long cracks in these alloys exhibited relatively constant, higher velocity, with extremely limited corrosion commensurate with oxidation of a free surface in this environment resulting in ~5 nm oxide layer.

1.0 Introduction

Al-Zn-Mg-Cu 7xxx series aluminium alloys have been of commercial interest since the 1940's, due to the benefits they offer to the transport sector as lightweight materials with high specific strength and good damage tolerance [1]. More recently, a newer generation of higher Zn-content alloys with lower quench sensitivity has been developed, targeting the aerospace sector for applications in thicker sections [2]. There is also interest in the development of even greater Zn content alloys, potentially providing higher strength materials [3]. However, significant challenges remain related to the environment-induced cracking (EIC) performance of these materials, which can be poor in a range of environments from immersed saline conditions to distilled water, as well as with humid air exposure [2, 4, 5 ,6, 7]. For example, their behaviour in humid air is currently of particular concern to the aerospace industry as has been highlight by a 2018 EASA safety bulletin [8].

In general terms, the EIC susceptibility of 7xxx alloys is associated with reactivity between water and the grain boundary microstructure under stress, which initiates and sustains crack propagation. Reactions between the environment and the grain boundary phases results in the absorption of protonic hydrogen (H) into the metal. Under a tensile load, this can lead to intergranular cracking caused by hydrogen embrittlement. The Mg containing ($Mg(Zn,Al,Cu)_2$) η-phase, which precipitates copiously on grain boundaries in 7xxx alloys (GBs) with a high area coverage, can anodically dissolve - if fully immersed - or react with water vapour, or thin surface adsorbed water layers [9], and is thought to be the main reactant in this process. Many metallurgical factors are known to affect the EIC performance of 7xxx alloys which are related to their bulk alloy composition and thermomechanical history, including; the composition and distribution of the grain boundary precipitates (GBPs) and

constituent phases, the presence of other reactive phase (e.g. τ and Mg_2Si), the grain structure and level of recrystallization, the matrix solute content and grain boundary segregation [10]. In particular, T7 over-aged tempers with two or more stages are preferred as they increase the Cu content and coarsen the distribution and spacing of the η-GBPs. However, in thicker plate materials the η-phase GBP populations are complicated by the low cooling rates which typically leads to two distinct families of precipitates; i) a coarser distribution of large- thin precipitates, up to 1 μm in length, that nucleate during quenching from solution treatment (Q-GBPs), grow on the GB planes with a complex branched morphology, and are richer in Al and Cu and lower in Zn, (as well as varying heterogeneously through a section thickness with the local cooling rate) and ii) a much finer distribution of ~ 50 nm scale ellipsoidal precipitates, which form at a lower temperatures on aging (A-GBPs) and are lower in Al and Cu and higher in Zn content [11].

A general understanding of EIC propagation in aluminium alloys in humid air is relatively mature, in terms of the factors that influence the crack growth rates and cracking mode; i.e. intergranular or transgranular [5, 6, 12]. There is a general consensus that for intergranular EIC of 7xxx alloys hydrogen-enhanced decohesion is the primary mechanism of crack growth [5, 6, 12, 13, 14], although the hydrogen enhanced local plasticity (HELP) [15, 16] and GB Hydrides [5, 10] are still deemed viable mechanisms that may contribute as changes to the alloy composition, temper, and exposure to different environments and different stress levels/states potentially present a wide spectrum of mechanisms that can be operative [17]. Caution is therefore required when attributing a single mechanism to a specific material. In addition, many aspects of the microstructural-stress-environmental interactions are still not well-understood. For example, the composition of the grain boundary precipitates is clearly important in determining their reactivity [18, 19, 20] and the ability to produce and adsorb hydrogen to sustain crack propagation [21, 22]. However, the GBP size, spacing, area coverage, and precipitate-free zone (PFZ) zone width as well as other factors have also been correlated with EIC performance of 7xxx series alloys (e.g. [10]). The grain structure (e.g. size, shape and aspect ratio) as well as second phase H trap sites also play a role [23, 24]. The composition, structure, and the nature of interface with the matrix of the GBPs can further affect their susceptibility to interfacial segregation of H and their decohesion behaviour, with recent atomistic modelling suggesting that H can reduce the η GBP-matrix interface cohesive strength more dramatically than that of the Al grain boundaries themselves, with and without GB segregation present [25, 26].

In reality, most of these microstructural factors are inter-connected and cannot be simply studied independently [10]. For example, over-ageing will increase the Cu content of the GB precipitates, but will also increase their size and spacing. Other effects, such as the dual populations of ageing and quench-induced precipitates [11, 18], further complicate isolating the most significant microstructural influence on performance. Overall, though, brittle intergranular cracking that follows high angle boundaries decorated with η precipitates (sometimes reported with a preference for recrystallized grain boundaries [27]) is the most important cited pathway for EIC in 7xxx alloys.

In contrast to long crack growth, initiation of EIC is less well understood, particularly in 7xxx series alloys. As defined by R H Jones [28] and R W Staehle [29] and later elaborated upon specifically for aluminium alloys [30], initiation consists of three mechanistically distinct stages before transition occurs to sustained crack propagation: i) *precursor, ii) incubation* and *iii) proto-cracks*. The ***incubation*** stage is where, on exposure to stress and the environment, **pre-cursor** features (including primarily surface defects, such as scratches, or microstructural features such as surface breaking pores and particles) with sufficient time develop to meet the conditions where cracking can first occur. Many contributing, sequentially-linked, processes may take place before the conditions for cracking are attained. Principal among the requirements is the creation of a stress concentrating feature [31, 32]

which if not already existing (e.g. as scratches or gas pores), can be created through corrosion, creep, or other time dependent processes. The creation of modified local environments within stress-concentrating features can lead to the generation of high local concentrations of H, until all the critical ingredients essential for cracking are achieved - so that EIC can nucleate and form ***proto-cracks***. These proto-cracks frequently remain undetected due to the limited temporal and spatial resolution of in-situ characterisation techniques and only once the cracks have grown into the short, or long crack, regime are they normally experimentally observed and measured.

Environmentally-driven chemical and/or electrochemical reactions within the restricted geometries generated during the pre-cursor, incubation and proto-crack stages of EIC initiation can also generate modified localized environment conditions [33, 34]. These localized environments can significantly increase the hydrogen fugacity by enhancing the corrosion reactions, where a locally concentrated stress can also assist the reactions, generating more H^+ that can be absorbed at a greater rate into the material [35, 36, 37]. In turn, the stress concentration developed by the feature will further affect the transport and accumulation of H^+ along grain boundaries to triaxially stressed regions that will become the proto-crack tip, once a threshold for cracking is achieved. The specific microstructure features and damage mechanisms that provide a pathway for proto-crack formation are thus important in understanding the crack initiation of 7xxx alloys [38, 39].

The focus of this study is thus to explore the initiation stage of EIC in new-generation 7xxx alloys in more detail, by exploiting a new in-situ optical monitoring approach, combined with a range of novel electron microscopy techniques, to obtain high resolution data precisely correlated to the different steps of crack development. This approach has allowed the stages of initiation to be unambiguously identified, along with the microstructural details of the initiation sites, which has shed new light on the mechanisms involved in the transition from precursor sites to sustained propagation of EIC cracks in these materials.

Experimental method

2.1 Materials and Sample Preparation

Two high Zn content new-gen alloys, AA7449 and AA7085, were commercially sourced in a T7651 temper condition as 95 mm and 140 mm thick hot-rolled plates, respectively. The bulk alloy compositions are provided in Table 1. The average grain sizes (area) determined by EBSD for AA7085 and AA7449 at this position in the L-ST plane were similar, ~ 5000 μm^2, with grain aspect ratios of 4.5 and 5, respectively [40]. The grain structures were predominantly fibrous with grains aligned in the rolling direction and contained ~16%, irregular shaped, recrystallized grains. Both alloys contained clusters of insoluble constituent particles distributed in bands, which were larger and predominantly Al_7Cu_2Fe in AA7449, along with a low volume fraction of Mg_2Si [11], whereas AA7085 had only a lower volume fraction Al_7Cu_2Fe.

60 x 15 mm wide, four-point bend (4PB) test samples were machined from the plates with their long axis aligned in the short transverse (ST) direction and their width in the rolling (L) direction. The samples were machined such that the middle position along their length (ST direction) was aligned at the T/4 plate position for AA7085 and the T/3 plate position for the less thick AA7449 plate, and after grinding and polishing the specimens were ~ 3.2 mm thick. A water- free final polishing was performed using isopropyl alcohol lubricant, with a sequence of 6, 3, 1 and ¼ micron polishing compounds, to prevent any corrosion prior to exposure to the test environment (more details can be found in the SI of [41]). The samples were thoroughly cleaned in an ultrasonic bath with isopropyl alcohol and warm-

air dried. Preparation of the samples was performed immediately prior to testing to limit exposure to the laboratory-air environment.

Table 1: Bulk alloy compositions from batch release certificates.

Alloy-temper	Plate gauge	Al (wt.%)	Zn (wt.%)	Mg (wt.%)	Cu (wt.%)	Fe (wt.%)	Si (wt.%)	Zr (wt.%)
AA7449-T7651	95 mm	Bal.	8.5	2.1	1.9	0.08	0.03	0.12
AA7085-T7651	145 mm	Bal.	7.6	1.5	1.7	0.04	0.03	0.12

2.2 Optically Monitored Four Point Bend Testing

Full details of the in-situ optical monitored 4-point bend (4PB) test procedure can be found in Ref. [42]. In brief, the samples were loaded in a stainless steel 4PB rig, using ceramic alumina rollers, with the displacement controlled to give a static surface tensile stress (at point of loading) of 75% or 85% of the yield stress at the start of the tests. The displacement was measured with a digital height gauge calibrated against strain gauge measurements. It should be noted that the maximum tensile surface stress for AA7449 at 75% yield (~ 390 MPa) was equivalent to that for AA7085 at 85% yield, owing to its higher strength. The yield stresses measured for each alloy at the test temperature of 70 °C were 520 MPa and 455 MPa for AA7449 and AA7085, respectively. 4 tests were conducted for each material/condition and analysed with multiples cracks and initiation sites investigated per sample.

After surface preparation and loading in the bend rig the specimens were immediately placed in a dry pre-heated Memmert™ humidity chamber for half an hour to thermally equilibrate before the humidity was slowly increased. All the tests were conducted at 70 °C and 50% relative humidity (RH). These conditions were chosen to remain in within the envelope of conditions that can be experienced in-service within an aircraft wing but at the top end so that the test is accelerated compared to lower temperatures. 50% RH was chosen to avoid the dew point and again within the in-service envelope of conditions. The test samples were continuously monitored in-situ using a custom, automated, optical, stage-motion system, designed to operate inside the humidity chamber, full details of which can be found in Ref. [42]. This system produced an optical map of high resolution (~1 µm) stitched images covering the full 15 mm width and the 25 mm length of the sample between the inner rollers of the 4PB test, with a frequency of 240 minutes per scan. The samples were monitored continuously until sample movement prevented this, typically samples were left a day or so after this leading to complete fracture of the samples. On failure, the samples were removed from the environment as quickly as possible and placed under vacuum until further analysis. A global-digital image correlation (DIC) technique [43, 44] was used to automate crack detection in the image maps, by exploiting the contrast from the coarse, second-phase, particles present in the images. This procedure provided large crack ID and crack length vs. time data sets, which are discussed more fully in ref. [42].

From this crack growth data the incubation time was determined by the point of first measurable increase in crack length. The length of transition from short to long cracks was estimated by fitting a straight line to the near-constant velocity long crack portion of the crack length vs. time data and an exponential curve to the remaining short crack data. The transition length was then defined as the last data point to be fitted by the exponential curve. The error in these values was estimated by halving the difference between the transition point length and the length of the preceding data point.

Another set of exposed samples was produced from cryogenically fractured (77 K) Charpy test samples, for surface oxidation analysis. As shown previously, the cold impact fracture was

intergranular-ductile [11] and exposed GB planes decorated with quench induced GBP's (Q-GBP's) and ageing induced GBP's (A-GBP's). The fracture surfaces where then placed in a humidity cabinet under the same conditions as the 4PB samples (i.e. 50% RH, 70 °C) for a similar test period of two weeks, with care taken to avoid any condensation by ramping up the temperature before increasing the humidity. These fracture surfaces were compared to those created by EIC.

2.3 Electron Microscopy Characterization

Secondary electron (SE) and (BSE) images of the fracture surfaces were taken with either a Tescan MIRA3 field emission gun (FEG) SEM at 5 kV (multiscale fractography) or at higher resolution with a Zeiss Merlin FEG-SEM operated at a low accelerating voltage of 3 kV (high resolution fractography). High-resolution low voltage (3 kV) energy dispersive X-ray spectroscopy (EDX) analysis of the fracture surfaces was also performed in the Zeiss Merlin FEG-SEM, which was equipped with an Oxford Instruments windowless X-Max Extreme, silicon-drift detector, which gave an interaction volume of < 50 nm in diameter.

TEM lamellar samples milled normal to the fracture surface through the oxide layer were prepared from selected samples using an Thermo Scientific Helios dual beam Xe^+ PFIB using a standard lift-out procedure after protecting the region of interest with Pt [45]. The lamella were thinned to electron transparency using successively lower ion beam currents at 30 kV, with a final cleaning stage at 5 kV and 27 pA ion beam current. Scanning TEM (STEM) imaging and energy-dispersive X-ray spectroscopy (EDX) elemental mapping was performed using a Thermo Scientific Talos F200X microscope, operated at 200 keV with a probe current of 180 pA and fitted with a FEI ChemiSTEM™ system. Spectral images were acquired and quantified using Thermo Scientific Velox software with an empirically fitted background correction and post-filtering applied.

To obtain information of the micron-scale porosity in the thick plate samples, a serial sectioned 3D data set previously reported was analysed, produced with a Thermo Scientific Helios 5 fs-laser-PFIB, fitted with an ultra-fast Oxford Instruments Symmetry EBSD detector. Full details of the automated serial sectioning procedure, reconstruction and analysis methodology are described in Ref. [46].

3.0 Results

3.1 Full crack lifetime observations

The in-situ scanning-optical monitoring system employed with the 4PB tests has previously been shown to be capable of unambiguously identifying the exact initiation sites of EIC cracks to a ~1 µm resolution, by back-tracking the time-lapse image sequence using large sample area maps [42]. By performing repeated optically monitored 4PB tests, the initiation and growth of 10's of EIC cracks have been tracked in real time using this technique [42]. Datasets showing example raw data are provided in Ref. [42] for the AA7449 and AA7085 4PB samples tested at the two different stress levels. Figure 1a shows an example set of results for AA7085 loaded to 85% σ_y and AA7449 loaded to 75% σ_y giving the same absolute stress of 390 MPa. Fig. 1b highlights the typical behaviour of a single dominant, primary crack, where 'Primary cracks' are defined as cracks that initiated in isolation from the influence of other cracks and 'dominant cracks' the primary crack that caused eventual failure of the sample. As described by Euesden et al. [42], smaller *'secondary'* cracks were also created within the stress field around the tips of large, primary, cracks as they propagated but they are not included in the crack growth measurements in Fig. 1.

Small initiating cracks could be first positively identified at the sample surface using the optical monitoring system when they became greater than 5 µm in length and their growth rates became

measurable after they had grown to 10-20 µm. When loaded to a starting surface stress of $0.75\sigma_y$, after introduction to the humid air environment, no visible surface changes typically took place for many hours with both alloys. Following this '*incubation period*', the first visible surface cracks appeared. Regardless of how they initiated, all the cracks then showed the same general behaviour illustrated in Figure 1. Following an incubation period before detection, the cracks first grew at a very slow rate with an erratic velocity and were probably arresting intermittently, although this was not detectable due to the time resolution, which was limited to 1 frame every 240 minutes. It is also worth noting that surface optical monitoring cannot clearly observe the proto-crack stage of initiation, but this was subsequently revealed by post-mortem analysis of the fracture surfaces (see below). At a length of 180-3000 µm (average, 800 µm) the cracks' growth rates then sharply accelerated (Fig. 1b), became more consistent, and entered a regime of near-linear length increase (i.e. near constant velocity) where no intermittent arrests were seen, although local regions of the crack front may still experience temporary arrest. This transition occurred when the crack length measured at the sample surface approximately equalled the grain size, which for these materials was ~600 µm in the crack growth direction (L) (Figs. 1 and 2). These two regimes are thus consistent with the classical definitions of a *short crack and long-crack behaviour* [47, 48] (see discussion). In all but one of the tests the first crack to initiate was found to go on to cause the final failure and were thus termed '*dominant cracks*'.

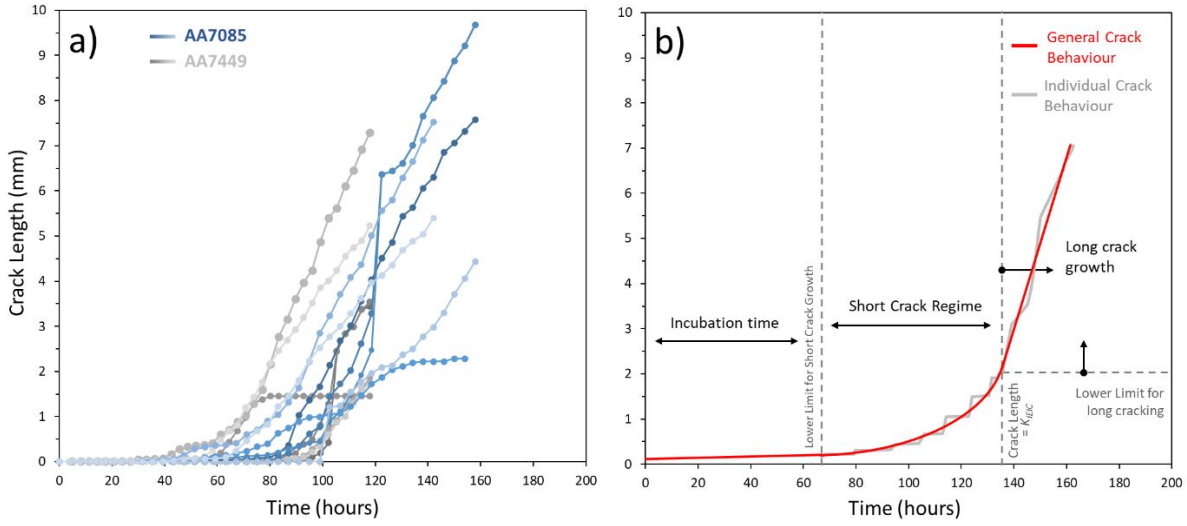

Figure 1. Crack growth measurements made with the optical scanning system showing (a) a selection of data recorded for primary cracks (replotted from [42]) for AA7085 $0.85\sigma_{0.2}$ and AA7449 $0.75\sigma_{0.2}$ (absolute stress =390 MPa) and (b) the typical behaviour of a single dominant-primary crack. The crack length equivalent to K_{IEIC} obtained from long crack DCB tests using linear fracture mechanics is also indicated on the graph [42].

This crack lifetime growth behaviour (e.g. Fig. 1b) was consistent for all the primary cracks in both alloys under the same test conditions (See Ref. [42]), although the overall EIC performance was worse for AA7449 compared to AA7085, which had a shorter time to failure in the 4PB tests, as has already been reported [2, 9, 42]. Fig. 2 summarises the incubation times vs the crack transition length to a long crack behaviour for the 9 cracks in each test. It can be noted that the cracks formed in AA7085 and AA7449 required a very similar average incubation time of: 56.98 hours compared to 58.70 hours, respectively. The AA7085 tests however showed a lower long crack growth velocity and took, on average, longer to transition to long cracks, by 102 hours compared to 82 hours. If we define the total initiation time to be the addition of the incubation time and the time for the short crack growth stage, it is clear it is the time for transition from a proto-crack to a long crack, rather than the incubation time, that is responsible for the difference between the two alloys to achieve sustained cracking when loaded to the same stress. For example, the cracks in AA7449 transitioned to long cracks at a smaller

average crack length of 0.38 mm, compared to 1.61 mm for AA7085, and even if the two very long outlier transition lengths for AA7085 are excluded the average time to the long crack transition was still double that of AA7449. In addition, the long cracks for AA7449 grew noticeably faster in the long crack regime at an average rate of 3.8 x 10^{-8} ms^{-1} compared to 2.3 x 10^{-8} ms^{-1} for AA7085, in good agreement with the larger dataset measured in [42], and for V_{II} plateau growth rates in DCB long crack tests [40]. In addition, when the incubation times were plotted against the transition crack lengths in Fig. 2, although the data is noisy, this suggests the longer the incubation time the shorter was the short crack regime.

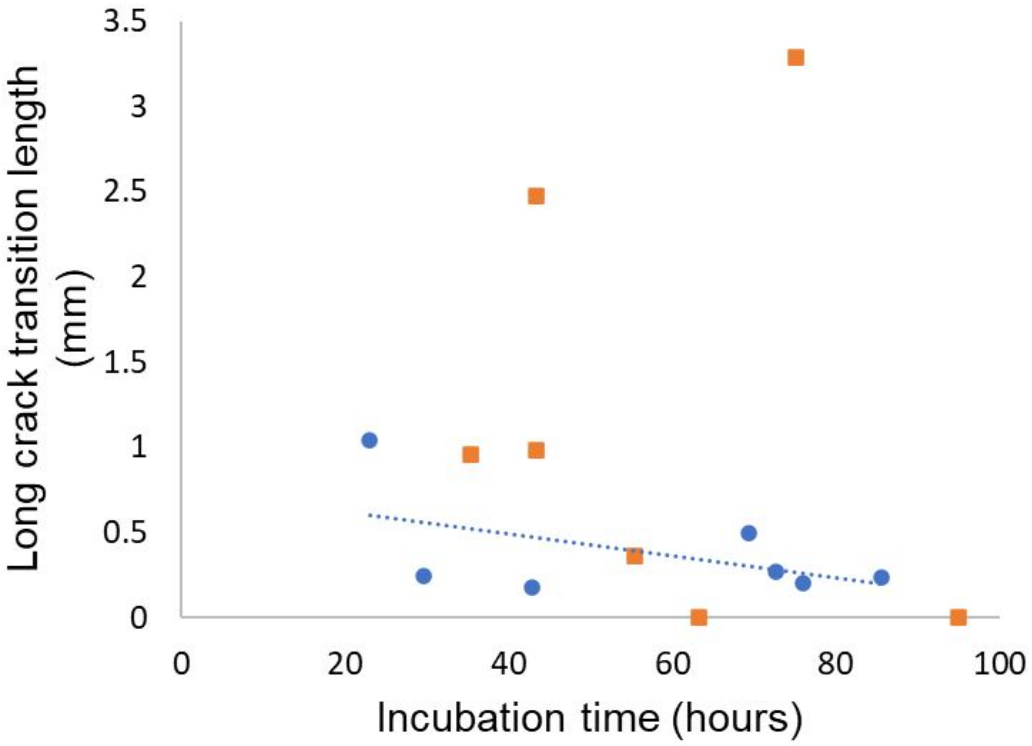

Figure 2. Data comparing the incubation times and long crack transition lengths from a short to long crack behaviour for 7 primary cracks in AA7449 (Blue circle data points) and AA7085 tests (orange square data points), performed at the same absolute stress level of 390 MPa. Linear trend line fitted to AA7449 data points.

3.2 Analysis of the Initiation sites

The in-situ optical-scanning monitoring technique, combined with face-matching SEM fractography and low voltage EDX oxygen mapping, was used to unambiguously identify the microstructural features that nucleated the *dominant* primary EIC cracks identified from the crack growth test data. Figure 3 provides an example of how the initiation sites were positively identified. These images also show that the fracture surfaces formed by EIC in humid air tests with these alloys with carefully preserved fracture samples are remarkably clean of corrosion products, with clean grain boundary facets and GBPs clearly visible [e.g. 9, 42], when compared to those subjected to more aggressive environments, such as following immersion in chloride solutions [e.g. 49]. In Fig 3 (a) – (c) little evidence of corrosion on the polished sample surfaces can also be seen in the optical images, which did not change significantly relative to the original condition during the test exposure period (<2 weeks). On the fracture surfaces (Fig. 3 d-f) the alloys' grain boundary topography is clearly visible in the SEM-SE images, with minimal plasticity apparent, and it is evident a highly brittle intergranular fracture process has developed that started immediately from the initiation site. Fig. 4 shows a further

eight typical examples of EIC initiation sites of dominant and primary cracks in the two alloys, selected from 10's positively identified by the same method.

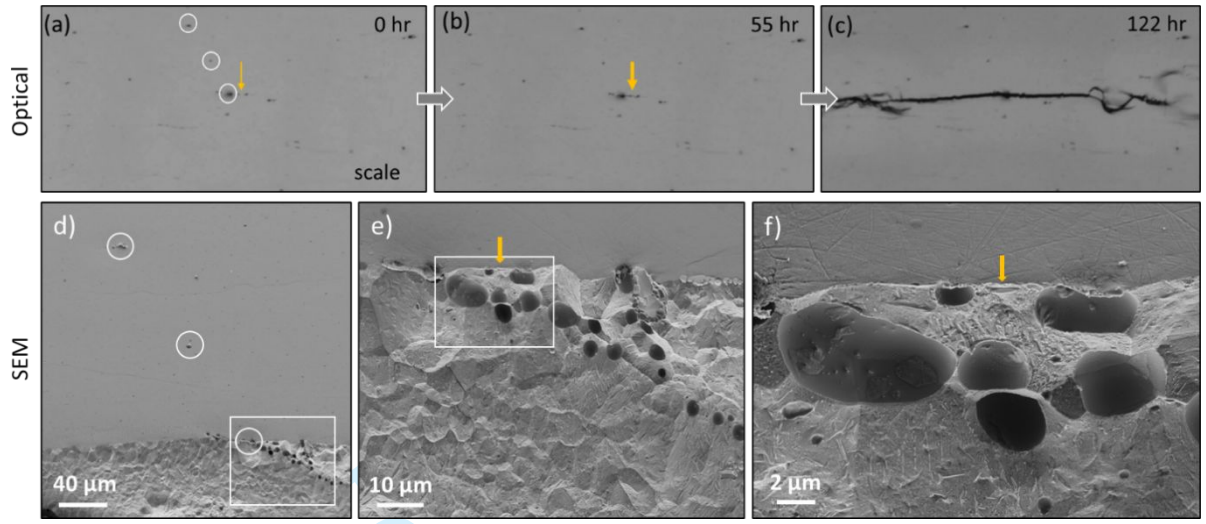

Figure 3. Example of the application of optical in-situ surface monitoring to unambiguously locate an initiation site in AA7085-T7651 tested at 50%RH and 75% σ_y, showing (a-c) Optical micrographs of (a) the initial surface condition, b) a small visible crack after 55 hours on test, (c) the longer crack after 122 hours. (d)-(e) provide secondary SEM images of the same location after the sample fractured correlated to the optical images (The same surface features are circled in white in (a) and (d). (e) and (f) provide Higher magnification views of the initial location of the surface crack (e). Yellow arrows indicate initiation site.

Importantly, *all* the primary crack initiation sites consistently revealed surface-connected, or very near surface gas pore-clusters, as an initiating feature. In most cases the pores were also combined with constituent particles, present as either large individual Mg_2Si particles, seen only in AA7449 (e.g. sites e)-g) in Figure 4), or polycrystalline clusters of Al_7Cu_2Fe, which were present in in both alloys (e.g. sites b) c) e) in Figure 4), but always co-located with porosity (see also Figure 3). Large Mg_2Si particles were especially prevalent at the initiation sites in AA7449 which were also associated with the gas pores. In addition, a lower fraction of initiation sites were found in each alloy (<10%) that did not involve any constituent particles, where initiation had occurred purely within a cluster of pores (e.g. Figure 4 a) & h)). However, these sites still contained large quench-induced η-phase particles [11] that grew on the interior pore surfaces and on the GBs connected to the pores, that after cracking initiated subsequently became the fracture surface. It should further be mentioned that the presence of surface-connecting gas pores at the initiation site were not necessarily immediately obvious from optical surface observation of the polished specimens, as they were often covered by a thin-perforated layer of deformed aluminium formed during metallographic sample preparation. The individual pores were also very small (typically <10 µm), often with only a small segment intersecting the surface, and were thus difficult to observe ab initio or distinguish from IMC particles by optical microscopy.

These small gas pores originate from the initial DC casting stage in the production of rolling billets and are caused by hydrogen, which is much more soluble in the molten metal, but has low solubility in solid aluminium, which is difficult to completely degas. Primary porosity consists of larger pores which form bubbles in the melt whereas secondary porosity emerges from the solid metal where it is dissolved. Primary pores can be healed during hot rolling to large plate reductions, but if not removed will tend to grow and spheroidise during high temperature solution treatment as shown by [50] secondary pores can also merge and coarsen during subsequent heat treatment to provide the

micron scale pores we see at the initiation sites.

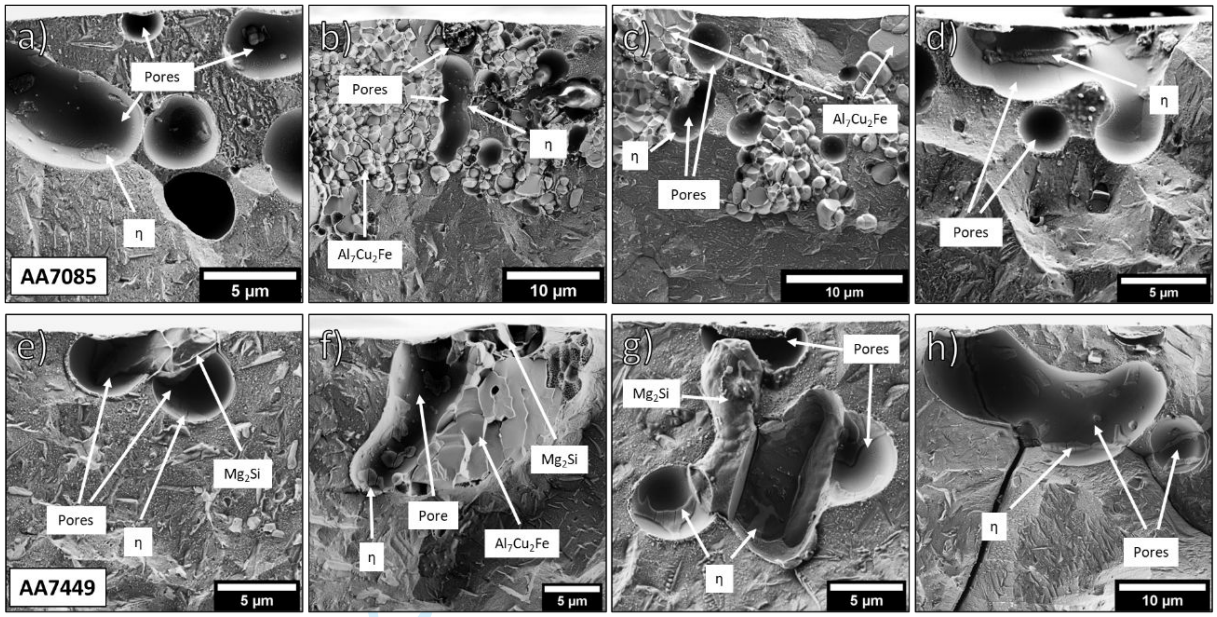

Figure 4. Secondary Electron images showing high resolution views of a range of initiation sites unambiguously located by in-situ monitoring, for dominant/primary cracks in AA7085 (a-d) and AA7449 (e-h), in 4PB tests exposed to 50% RH at 70 °C. All present a surface breaking pore cluster and all, apart from a,) in combination with coarse constituent particles.

Identification of the point of initiation

Once the location of the initiation site was identified from the optical time lapse images, low energy windowless SEM-EDX, was applied to study the same area immediately around the initiation site on the fracture surface. The point of initiation could then be revealed more precisely from its associated elevated oxygen signal. Figs. 5 and 6 present a detailed analysis of one of the rarer initiation sites in the AA7085 alloy (Figure 4a) that occurred without any constituent particles present. More typical initiation sites, which featured co-located coarse constituent particles and pore clusters, are also investigated in Figure 8 and Fig. 9. Although initiation was more commonly observed within, or at the edge of a constituent IMC particles-clusters associated with pores, it is easier to first interpret the evidence for the typical initiation sequence without the presence of constituent particle clusters which introduce more complex fracture features.

Initiation sites without constituent Particles/Clusters

In Figure 5b, an overview low-voltage EDX spectrum oxygen map is provided of a rarer constituent particle-free pore cluster initiation site in AA7085. The low energy EDX reveals three distinct regions on the fracture surface at the initiation site: i) a *very* small ~5 µm diameter region of elevated-uniform oxygen signal, which is highlighted by the white box in Fig. 5b-c) and shown enlarged in Figure 6; ii) a larger roughly semi-circular area surrounding this region, exhibiting an elevated oxygen signal in a concentric ring pattern that radiates out from the initiation site to a distance of ~50 µm (marked in yellow in Fig. 5a) which contains crack arrest markings (CAMs) see Fig. 5c [5, 51, 52]; iii) further away from the initiation site, the surrounding area is covered with a more uniform thinner oxide layer without any CAMs present when observed at this magnification. In all these locations the oxide appears thicker locally over exposed η-phase grain boundary precipitates compared to the exposed aluminium matrix. However, it should be emphasised that overall the oxide layer was very thin and could only be successfully imaged with this level of detail using a low voltage windowless detector. Fig. 5f shows the relative change in O-signal from the initiation site into the CAM region.

In this example (Figure 5) the point of initiation indicated by the area of greatest and more uniform oxygen signal is located between three neighbouring gas pores that are slightly subsurface within an elongated band of pores that have formed along a grain boundary that intersects with the polished surface. Although the initiation point is slightly subsurface, the pore immediately above the oxidised ligament is connected to the surface. Locally this has created a small sub-surface metal ligament that would have been highly stressed (see white arrow in Figure 5c). This ligament also has a GB running through it, which later became part of the exposed fracture surface. At this exact location there were no large constituent IMC particles present, although there is an Al_7Cu_2Fe cluster touching a nearby pore from the same cluster that intersects the surface to the right of the initiation site, this did not initiate the crack. This large gas pore cluster along a grain boundary, which intersected the sample surface, has resulted in this location becoming the preferred site of initiation in this sample; i.e. it formed the feature that led to the shortest initiation time and developed into the dominant EIC crack that caused sample failure in this test. It should be noted that whilst no coarse constituent particles were involved in this example, large Mg-rich η-particles are apparent on all the pore surfaces and on the connecting grain boundaries (Fig. 6).

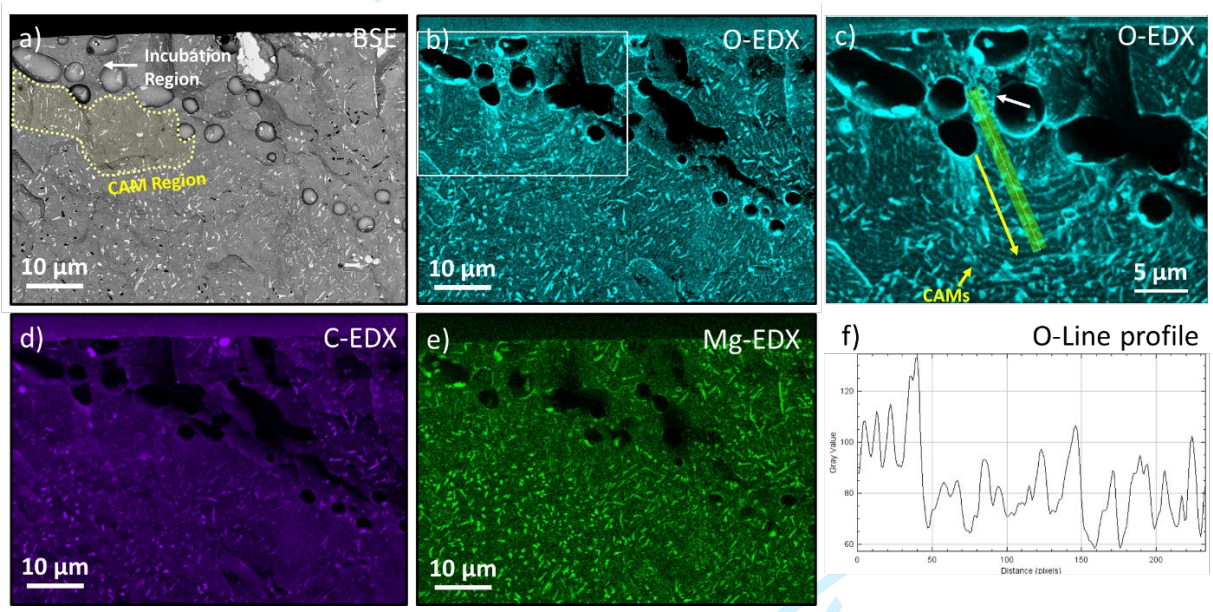

Figure 5. Example of an initiation site identified for the dominant crack in a 75% σ_y loaded AA7085 4PB test sample that occurred within a pore-cluster: a) Backscatter electron image and b) a low energy EDX spectrum map for oxygen that reveals a small region of elevated oxidation at the point of initiation(white box) shown in c) Magnified region of O EDX map highlighting CAM's and location of line profile indicating relative O- signal (f). d-e) show C and Mg EDX spectrum maps highlighting the distribution of grain boundary η-phase and their reaction with C, suggested to be $MgCO_3$.

Evidence for corrosion at the initiation site

Figure 6 provides an enlarged view of the extremely small initiation region that is only a few microns across, where a locally elevated oxygen signal was highlighted by the white box in Figure 5b. At this magnification the SE image reveals a rougher surface compared to the rest of the crack, covered by an irregular and more substantial oxide film that contains degraded η precipitates, which is suggestive of chemical attack. Comparison of the Cu, Zn and Mg, EDX spectrum maps in Figure 6b-d) provides evidence that in this region the η-phase $Mg(Zn,Al,Cu)_2$ particles have been nearly completely leached of Mg and most of their Zn, which are their more reactive elements. As highlighted by the example indicated by the yellow-dashed ellipse in Figure 6b-e), the original elongated morphology of the exposed η particle is only evident in this region from a residue of Cu-rich particles seen at the location it formerly occupied and there is little detectable Zn or Mg remaining locally. The white and red circles

in Figure 6e) provide examples of other locations where a former GB η-precipitate was slightly less severely chemically attacked, with some Mg and Zn still detectable at the prior precipitate site. Again, Cu nanoparticle remnants can be seen on the surface. In addition, a large η particle that has been chemically attacked can be seen at the top right of these images within the surface-connected gas pore that exhibits corrosion products and smearing of the Mg across the pore surface associated with an elevated O signal.

Further STEM-EDX evidence of the chemical attack of the η phase precipitates at the initiation site is provided in Figure 6f-k) from FIB cross-sections milled out of the fracture surface at the location indicated in Figure 6a). These images show at higher resolution that the η phase particles in this region have fully dissolved, with only Cu remaining near the original precipitate site, which now has no co-located Mg and Zn. The Mg and Zn has been completely leached out of the η particles in this region to be dispersed across the surface and incorporated into the oxide layer. The oxide layer across the Al-matrix in this incubation region was also thicker compared to the long crack region of the fracture surface (see below), with a maximum thickness of up to 38 nm and an average thickness of 26±8 nm and can be seen to be enriched with Mg and Zn (see Table 3 and Fig. S1 and S2 in SI for measurement method).

Overall, the appearance of the fracture surface in this region is thus consistent with the selective dissolution of elements from the η-phase particles and their redistribution by ionic transport; suggesting that a liquid water layer of reasonable thickness must have resided in this location for a sufficiently long time to result in these features. Evidence of water condensed within surface fissures was also observed, on the surface of some samples after 4PB testing. For example, in Fig. 7 surface staining can be seen surrounding a cracked Mg_2Si particle in a AA7449 sample that had not initiated an EIC crack (probably because it was not co-located on a GB) that is indicative of liquid being expelled and leaving a residue once the sample was introduced to the vacuum of the SEM.

As highlighted in Fig. 5c and d, in the region surrounding the initiation site, some of the η phase precipitates were also consistently associated with a carbon signal from the EDX spectrum maps. Dark, nearly black, patches were also be seen obscuring some of the bright BSE contrast of the η precipitates, which were determined to have a high local C signal. This is therefore likely to be evidence of the presence of some magnesium carbonate ($MgCO_3$) which has formed due to reaction under the conditions of lower pH involving the generation of anionic species, namely carbonate and bi-carbonate ions (CO_3^{2-} & HCO_3^-, respectively), which are available to support local electrochemical reactions and corrosion processes following the dissolution of atmospheric CO_2 into a water layer that formed on the fracture surface under these high humidity conditions, as discussed later. These carbonate and bicarbonate species may be necessary to support local electrochemical reactions and corrosion processes to generate the nano particle copper deposits observed in Fig. 6.

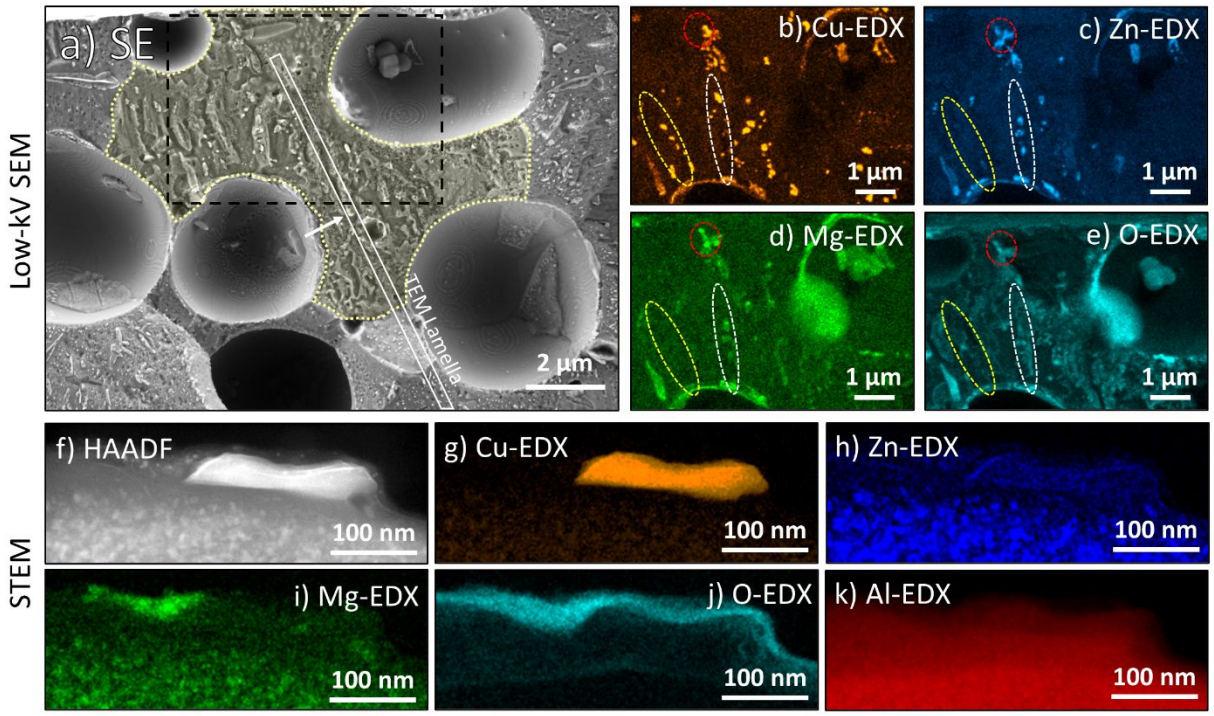

Figure 6. Higher magnification analysis by SEM-EDX and STEM-EDX of the AA7085 initiation site shown in Figure 5: a) SE image with the incubation region highlighted in yellow; b-e) low-kV EDX maps showing a magnified view of the region highlighted in black in (a). The three highlighted regions show η-phase precipitates in varying states of chemical attack. The yellow-dashed ellipse in (b)-(e) highlights a precipitate which has undergone near total dissolution, with only Cu clusters remaining. The dashed-red ellipse and white circle indicate a precipitate that is partially dissolved, with a reduction of the Mg/Zn signal and the Cu content remaining; In f) -k) STEM-EDX images are provided from a FIB lamella sample that cuts through the site of a η-phase Q-GBP depicted in (a), at the point indicated by the white arrow; f) a High Angular Dark Field Image (HADF) and g)-k) EDX maps showing total dissolution and dispersal of Mg and Zn as well as a locally thicker (~100 nm) corrosion product.

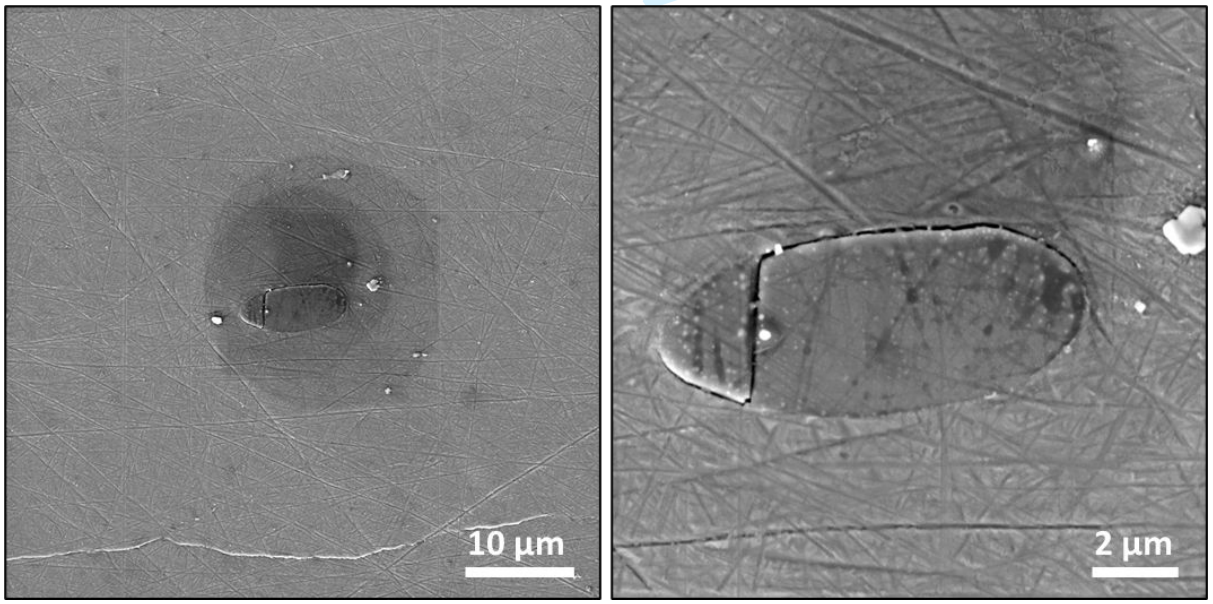

Figure 7. SE SEM image showing evidence of surface staining on a AA7449 sample following exposure to 50% RH and 70 °C suggesting some water condensation around/within the fissure formed between a Mg_2Si particle and the aluminium matrix. The liquid was expelled on to the surface once the sample was introduced to vacuum in the SEM.

Table 3. Average oxide thickness measurements performed on the aluminium matrix and η phase particles in a AA7085 sample as measured by STEM-EDX. Table compares samples subjected to 4PB testing and those fractured cryogenically to

expose the grain boundaries using Charpy impact and then exposed to the same environment. The measurement method is shown in Figs. S1-S2.

	Test	Feature (Location)	Oxide Thickness (nm)	
			Mean	Std. Dev.
Fig. 6	4PB @ 70 °C, 75% σ_y, 50% R_H (~2 weeks)	η Precipitate (incubation region)	26.16	8.30
Fig. 6	4PB @ 70 °C, 75% σ_y, 50% R_H (~2 weeks)	Matrix (incubation region)	15.45	6.32
Fig. 10	4PB @ 70 °C, 75% σ_y, 50% R_H (~2 weeks)	CAM (adjacent to incubation region)	26.62	5.11
Fig. 11	4PB @ 70 °C, 75% σ_y, 50% R_H (~2 weeks)	Matrix (> 1mm from initiation site)	3.93	0.57
Fig. S3	4PB @ 70 °C, 75% σ_y, 50% R_H (~2 weeks)	η Precipitate (> 1mm from initiation site)	13.74	3.05
Fig. 11	Charpy → 70 °C, 50% R_H (2 weeks)	Matrix (arbitrary location)	5.45	1.35
Fig. 11	Charpy → 70 °C, 50% R_H (2 weeks)	η Precipitate (arbitrary location)	17.12	5.46

Initiation sites with collocated constituent particles and gas pores

Images from the more typical, but more complex, scenario of an initiation site where gas pores are co-located with large constituent particles are provided in Figure 8 and 9, from dominant cracks found in AA7449 and AA7085 4PB test samples, respectively. In Figure 8 both a smaller Mg_2Si and a large polycrystalline Al_7Fe_2Cu particle, exposed to the polished sample surface, were identified at the initiation site. The Mg_2Si particle exhibits an elevated oxygen signal in the EDX map (Figure 8b), suggesting it had been corroded. Interestingly, constituent Mg_2Si particles were frequently found to be associated with the initiation sites in AA7449, but this phase was not present in the AA7085 alloy owing to the lower Si level. The large Al_7Fe_2Cu particle at the AA7085 initiation site has fractured open in the same plane as the pore and there is also an elevated oxygen signal surrounding this particle. However, the Al_7Cu_2Fe particle itself does not appear to have been oxidised due to its more noble constituent elements.

The probable 'point of initiation' indicated by the red arrow in Figure 8a is where the grain boundary plane connected to the gas pore would have first been penetrated by a small fissure and it is probable this followed fracture of the IMC cluster, which would have created a sharp crack that provided a high stress concentration and promoted liquid water condensation within it. Further evidence, although more difficult to see in this example because of the more complex fracture surface, is the presence of CAM's surrounding the oxidised initiation point, indicted by the yellow dashed arrows in Figure 8b. At this site there is no other nearby pore to create a vulnerable ligament of metal. However, the pore was relatively large and deep, is intersected by the sample surface, and has formed next to a hard IMC particle will have increased the stress concentration acting at this site.

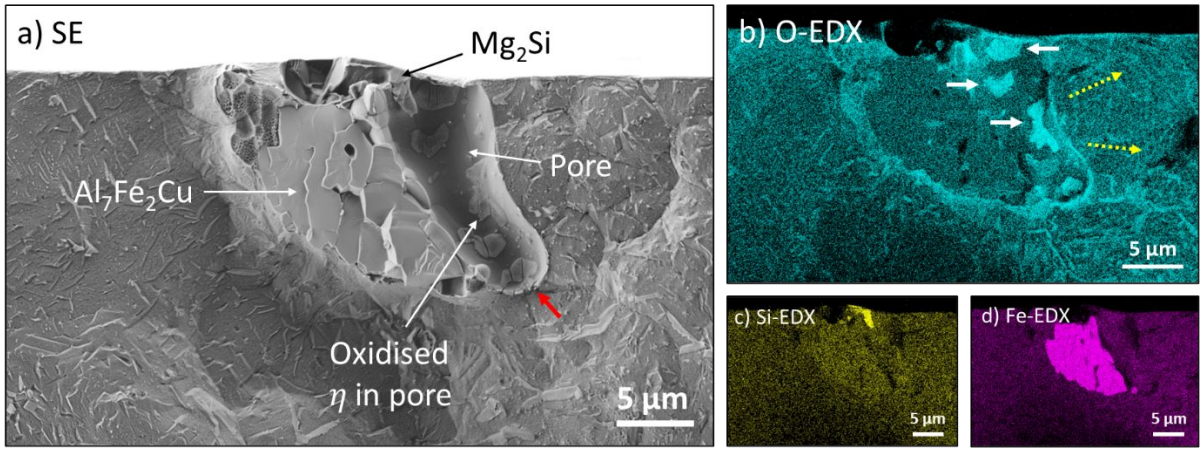

Figure 8. Example of a typical dominant crack initiation site for an AA7449-T7651 4PB test loaded to 85% σ_y showing; a) a SE image with red arrow indicating the probable point of initiation, accompanied by EDX spectrum maps of b) O, c) Si and d) Fe. White solid arrows show regions of elevated oxygen signal, yellow dashed arrow indicates region and direction of CAMs.

Apart from the absence of a Mg_2Si particle, a similar behaviour was seen at another typical initiation site in AA7085 - as shown in Figure 9. In this example, a larger polycrystalline aggregate of Al_7Cu_2Fe is seen surrounding a cluster of embedded gas pores, which has acted as the initiation site. Using the same EDS oxygen signal method as described above, we can also identify a probable point of initiation (red arrow in Figure 8a) which again occurs at a ligament of metal that separates two sub-surface gas pores. One intriguing aspect here is that this point of initiation is below the surface and at first site does not appear to be directly associated with a surface breaking pore. However, as indicated by the black arrow in Figure 9a, there is an immediately neighbouring surface pore that is filled with some detritus, which is not Fe or Si rich and we assume came from the polishing process. The ligament of metal connecting this surface sectioned pore to the sub-surface pore that includes the point of initiation, is exceptionally thin and within a couple of microns of the surface. The local elevated oxygen signal again suggests that this ligament was broken, either upon mechanical loading or possibly through a corrosion reaction, or a combined stress-assisted corrosion mechanism, albeit with very minimal corrosive attack. It is also highly likely that such a large Al_7Cu_2Fe-pore aggregate had already cracked during rolling, or during loading the sample and this allowed access to the environment, as well as creating a large stress concentration in the ligament upon loading.

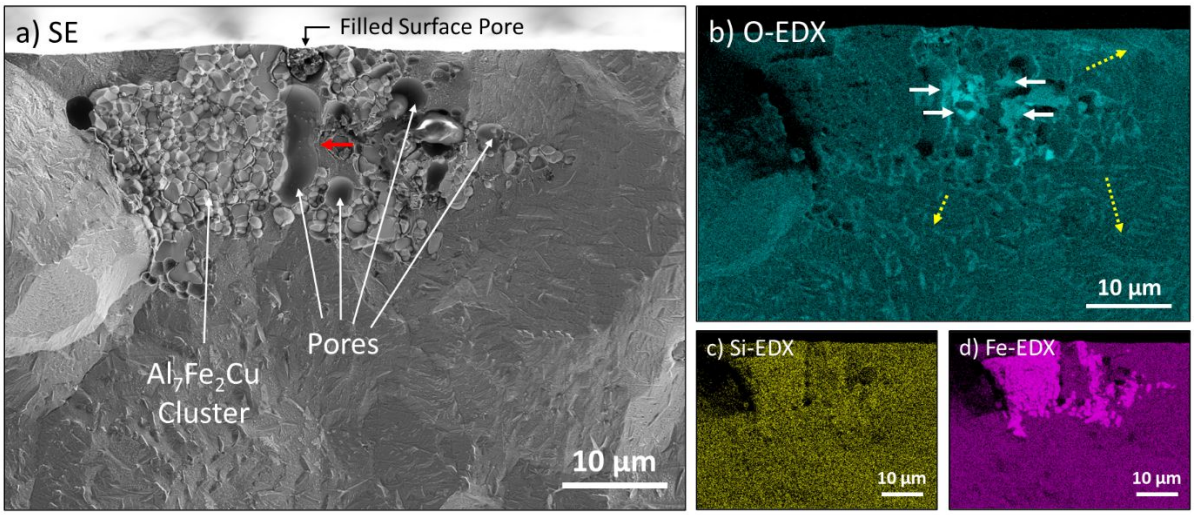

Figure 9. Example of a typical dominant crack initiation site for an AA7085-T7651 4PB test at 85% σ_y at 70 °C and 50% RH, viewed at higher magnification, showing a) SE image with the red arrow indicating the point of initiation; EDX maps of b) O, c) Si and d) Fe. The yellow dashed arrows indicate the local direction of CAM's movement.

3.3 Gas pore initiation features

It is revealing to examine the interior of surface connected gas pores, that acted as crack initiation sites in all cases, more closely. In Fig. 10, a further example from a rarer AA7449 constituent particle-free initiation site is provided (from Figure 4h). It can be seen that the large gas pore next to the initiation point is situated at a GB triple point and all of the intersecting GB's exhibit cracking. The intact GB's highlight exposed large quench-induced η-phase precipitates on the GBs intersecting the pore. The higher-resolution face-matching images also reveal that these fractured η-phase precipitates show evidence of reaction products, suggesting some localised corrosion has occurred within the pore (note the dark staining to these otherwise bright relatively high atomic-number particles). From the higher magnification face-matched insets (Fig. 10 d-e) there is also some evidence of topography in the matrix that does not correspond to impressions made by corroded, or missing particles separated from either half of the fracture surface. This therefore appears to be evidence of corrosion following local plastic deformation. There are also some tiny square-shaped pits in the aluminium matrix and in the gas pore, which could be caused by the dissolution of finer η A-GBPs. As an aside point of interest, fine regular steps which appear like 'contour' lines can be seen on the pores' interior surfaces. These lines are crystallographic steps resulting from faceting of the pore surface that occurred to reduce its surface energy during the high temperature solution treatment (Fig. 10 b-c).

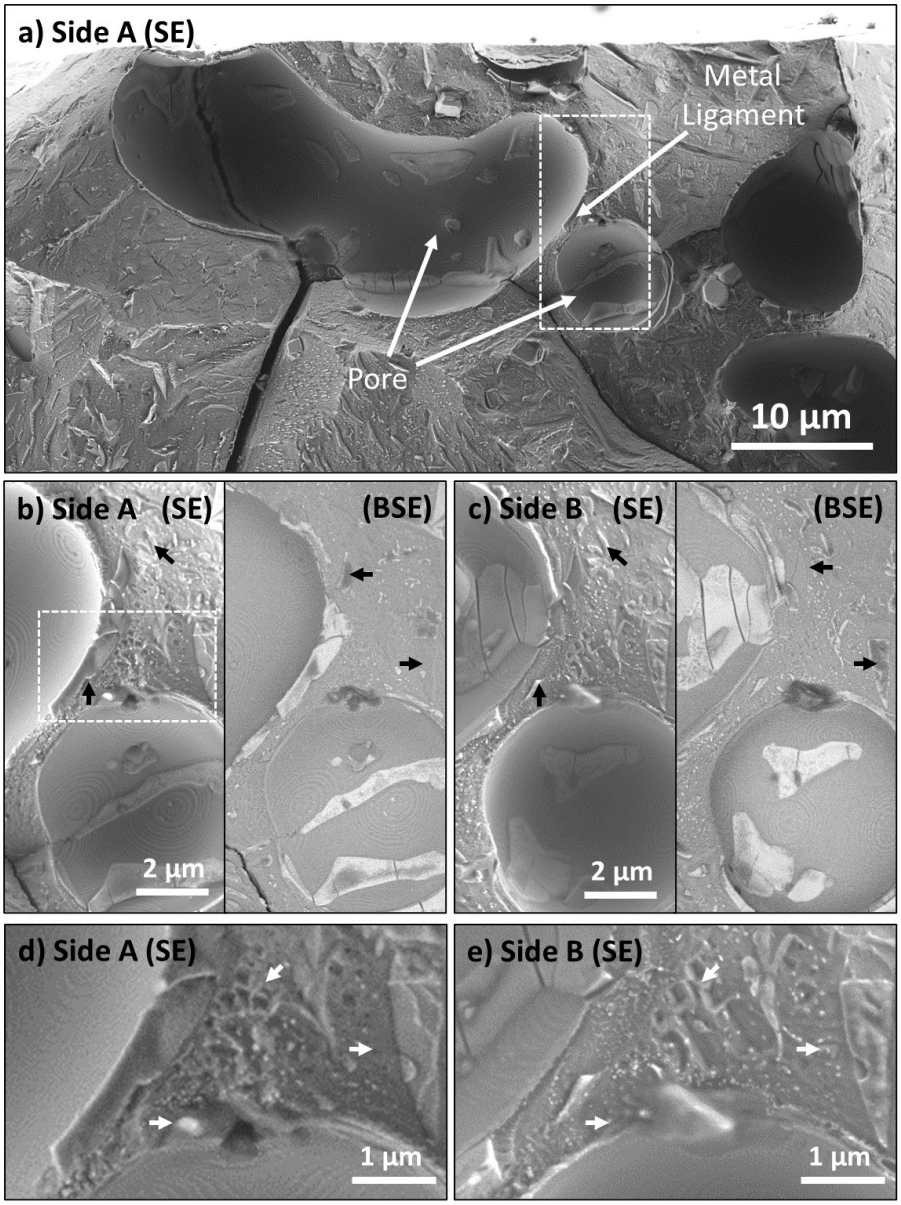

Figure 10. Higher magnification views of the pore cluster AA7449 initiation site, shown in Figure 4h): a) SE image showing multiple pores and a small ligament of metal believed to be the initiation site; b, c) face-matched SE and BSE images showing the area highlighted in (a); d, e) SE images of the area highlighted in (b). Black and white arrows mark areas which appear well and poorly matched, on opposing sides of the fracture surface, respectively; d, e) higher magnification views of the region highlighted in (b). White arrows show possible crystallographic pits at a very fine scale.

3.4 CAM Regions

The CAM regions identified in the low-voltage oxygen EDX maps in Figure 5, were studied in more detail by higher resolution imaging of the fracture surfaces using FIB-prepared lamellae cross-sections of the fracture surface using STEM; as shown in Figure 11. In Figure 5,Figure 8, and 9, although difficult to see in some images, regularly spaced CAMS were apparent on the fracture surface surrounding the initiation sites. These features were visible in the low voltage SEM oxygen signal EDX maps because they formed bands of thicker oxide. Closer inspection in Figure 11 shows that the bands were composed of local regions where, on average, more chemical activity occurred and a thicker (although still relatively thin <30 nm) oxide developed. For example, in the high magnification SEM images in Figure 11c it can be seen that locally there are more small pits along the CAMs, where small ageing-induced η-precipitates have fully dissolved, and there is also a local accumulation of Cu nanoparticles

within the CAM bands compared to that present across the fracture surface between the band intervals, or further away from the initiation site.

STEM analysis of a FIB sectioned lamellar cut through a CAM in Figure 11 d) –i), confirms that almost complete dissolution of the A-GBPs has occurred along the CAM band lines, as only Cu nanoparticles can be seen in their place without any Mg or Zn present, suggesting extensive selective dissolution of the η-phase and re-precipitation of small amounts of dissolved Cu. The average spacing of the CAM's was measured as 803± 13 nm in reasonable agreement to that seen in AA7050 under similar conditions [5, 24]. In addition, the higher resolution cross-section STEM images in Figure and 12 show a thicker oxide (~26 ± 5 nm) across the CAM line (see the summary data in Table 3). The CAM line is also enriched in Mg and Zn dispersed across the surface away from the η-phase precipitates where the oxide thickening has occurred. In comparison, between the CAM lines, and in regions away from the CAM's (see Fig. 12) the oxide thickness was only ~5 nm and the A-GBP η particles were still intact and less attacked, showing only near-surface leaching of Mg. While it must be emphasised that this oxide layer is still very thin and the size of the reaction region and extent of surface reaction is very much smaller, compared to that seen under fully immersed conditions (e.g. [49]), the CAM's and the point of initiation that they surround both display evidence of highly localised corrosion with ionic transport, which is indicative of a liquid water layer; i.e. this micron-scale water meniscus was thick enough to allow leaching out of Mg^{2+} and Zn^{2+} ions and disperse them away from the η GBPs as well as re-precipitation of small amounts of Cu as nanoparticles.

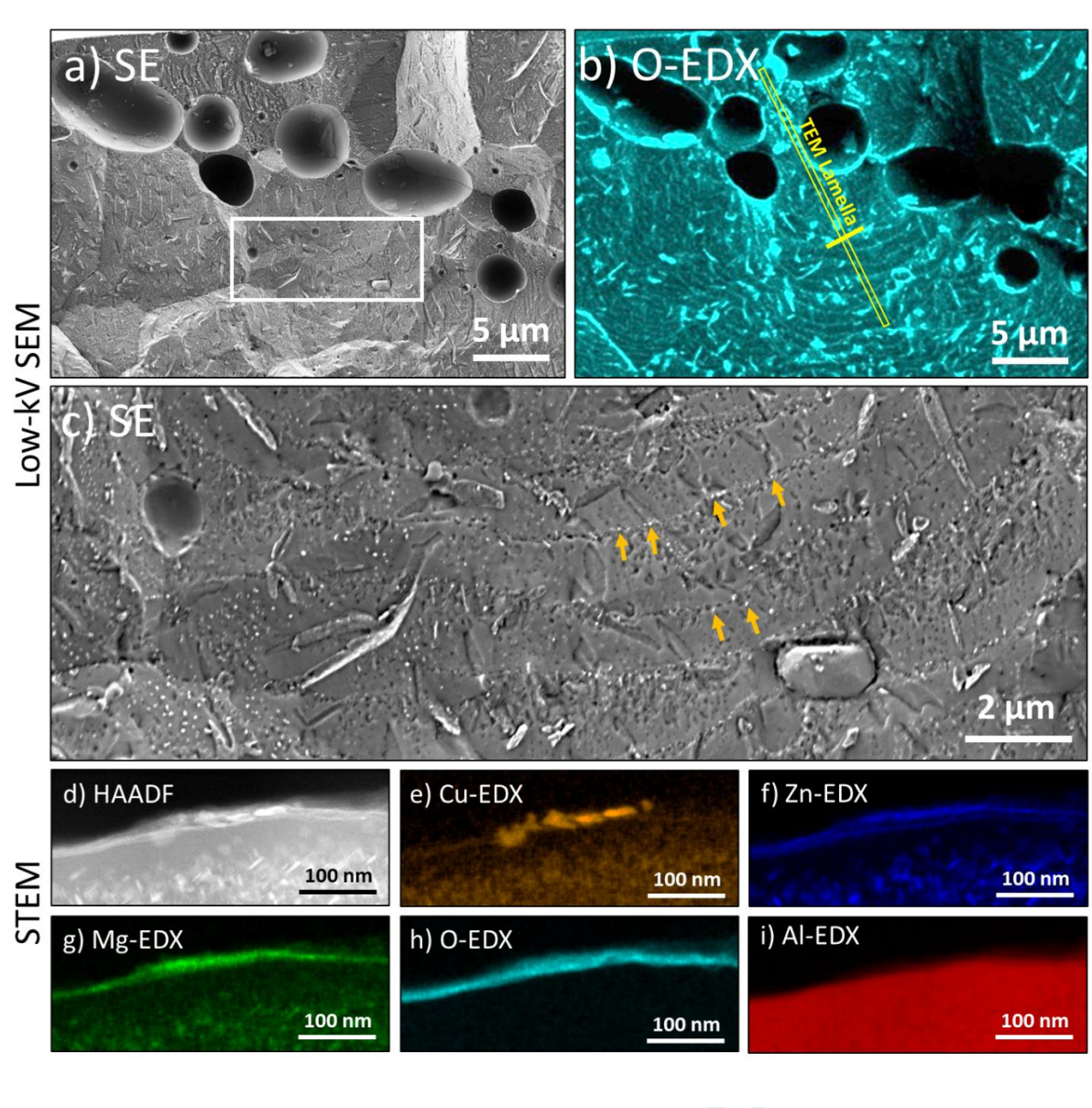

Figure 11. STEM-EDX results of the CAM region adjacent to the AA7085 initiation site shown in Figure 5, 6 a) SE image and b) O-EDX maps showing the CAMs, with the location of the lamella highlighted in yellow; c) magnified SE image of the CAM's showing bands of corrosion activity and Cu nanoparticles d-i) HAADF image and STEM-EDX maps showing a cross-section of a CAM line at the point indicated in (b). The maps show a subtle enhancement of the local oxide thickness, incorporation of Mg and Zn dispersed from the η-phase and corroded matrix with a residual Cu nanoparticle.

3.5 'Long Crack' Rapid Propagation Region

Within the short crack regime, after distances of only over 50-100 µm from the initiation site, the oxide layer become thinner and more uniform on the fracture surfaces and the CAM lines faded below the limit of SEM-EDX detection (Figure 5, 8, and 9). Using a simple linear-elastic analytical approach [53] with a 50 µm half penny, crack length the stress intensity of the crack is estimated to be ~2 MPa√m [42] and with a 100 µm crack K increases to ~2.9 MPa√m, at this applied stress level, which is still considerably below the K_{IEIC} threshold of 6-7 MPa√m measured in long crack falling K DCB tests for this alloy [40].

The level of oxidation seen across the rest of the fracture surface in the long crack region was also investigated further by TEM using FIB-lamellar cross sections, extracted from a position ~1 mm from

the initiation site. These results were cross-referenced to samples similarly exposed, to 50% RH humid air at 70 °C for 2 weeks, that had been cold fractured using a Charpy test to expose the grain boundaries. When carefully compared (Fig. 12), the TEM samples from both these fracture surfaces showed a very similar, thin, uniform oxide of equivalent thickness across the aluminium solid-solution matrix regions of 5.5 ± 1.4 nm (see Table 3). On both samples the GB η-phase particles that were exposed by fracture were still largely intact but had locally thicker oxide layers that were very similar in thickness (~15 nm) and exhibited more local enrichment of Mg and some 'spots' of Zn in the oxide. In addition, in these samples the Mg incorporated into the oxide layer did not significantly disperse away from the location of the η particles which were only partially reacted with the environment. Overall, these results thus indicate that further away from the initiation sites, within the long, rapid crack propagation regime, the chemical activity was very localised to a thin layer on the exposed fracture surface and there was no longer any clear evidence of corrosion processes requiring a liquid water layer capable of ionic transport. Comparison to the cryogenic fracture surfaces, which were subsequently exposed for a similar time, also suggests that there was nothing 'special' about the occluded EIC crack tip environment for long cracks as the level of oxidation/corrosion is equivalent to that seen to a free grain boundary surface exposed to the same environment.

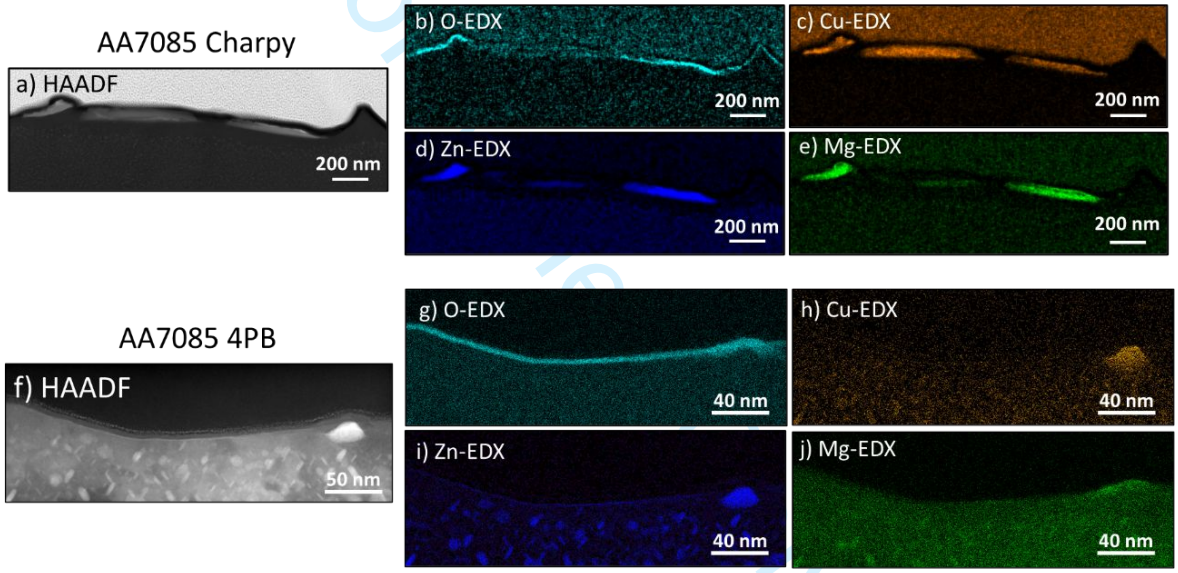

Figure 12. a) & f) STEM results from Charpy-tested AA7085 samples exposed to humidity post-fracture and long crack fracture surface following 4 point bend testing under the same environment. b-e) & g-j) STEM-EDX maps of O, Cu, Zn and Mg for the two test samples.

3.6 Statistical analysis of pores clusters

Following the discovery that clusters of small gas pores were the main initiation sites, an investigation was performed into the prevalence of gas pores in the hot rolled thick plates. Because of their small size, a fs-laser serial sectioning 3D dataset of the AA7085 alloy was collected and analysed. Full details of the novel technique used to generate and reconstruct this data is provided in Ref. [46]. Fig. 13 shows the distribution of gas pores at the T/4 position. A number density of 4.9 x 10^{-6} µm^{-3} was found in the 0.15 mm^3 volume analysed with an average pore diameter of 2.9 µm. Although the total volume fraction of the pores was only 0.009%, as can be seen from Fig. 13 most of the pores were concentrated in clusters aligned by rolling, where locally they were in close proximity to each other with a spacing of the order of a pore diameter. The pores also generally appeared alongside intermetallic particles and were predominantly found on grain boundaries (see Fig. 13b).

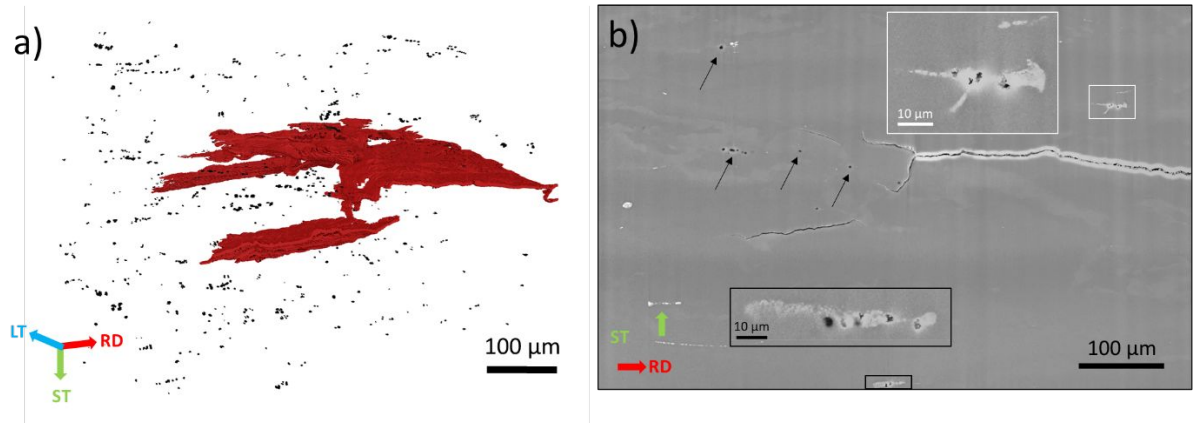

Figure 13. (a) Volume rendering from fs-Laser serial section data showing the distribution of small gas pores near a rendered crack tip and (b) a magnified SE-SEM slice from the 3D data set showing pores (black arrows) associated with IMC particles (inset images), within the AA7085-T7651.

4.0 Discussion

4.1 AA7449 and AA7085 EIC initiation performance

By exploiting time resolved in-situ sample monitoring, combined with detailed fractographic and high-resolution chemical analysis, higher fidelity information has been obtained than previously published on the early stages of EIC initiation and its transition to sustainable crack propagation, on humid air exposure of two EIC-susceptible new generation 7xxx alloys. These two alloys have been studied in parallel to see if the same processes apply generally across similar Al-Zn-Mg-Cu alloys with high Zn contents. In recent work, these two materials have shown high, but different, rates of initiation in conventional humid air static load tests and long crack growth rates in DCB tests, with AA7449 initiating propagating cracks faster, which then also grew as long cracks at a slightly higher rate than in AA7085 [2, 7, 42, 54]. AA7449 also had a slightly higher threshold stress intensity, K_{1EIC}, than AA7085 [43]. Here, both alloys have been found to exhibit similar types of initiation site and the same general initiation behaviour and stages of transition to sustained crack propagation. Although the incubation times required to develop a proto-cracks in AA7449 and AA7085 were similar, AA7449 was found to exhibit a significantly faster transition from a short to long crack behaviour compared to AA7085, when tested under the same humid air conditions (50% RH) and again had higher long crack growth rates in the 4PB tests.

There are two major aspects which explain this different EIC performance. Firstly, there are more constituent particle clusters in AA7449, which also contains larger Al_7Cu_2Fe particles, and secondly AA7449 contains a low density of more reactive Mg_2Si particles. In comparison, AA7085 contains less Fe and a higher ratio of Zn to Mg and thus fewer and smaller constituent particles, which are comprised almost exclusively of Al_7Cu_2Fe [2,9,11]. The presence of more constituent particles may also mean more gas pores as they are associated with the constituent particles. However, AA7449 was produced as a thinner (95 mm) plate and has been subjected to a greater rolling reduction. Further work is still needed to examine the comparative pore distributions in this alloy using the same 3D serial sectioning technique. Nevertheless, AA7449 contains Mg_2Si which was found at a majority of its initiation sites. This phase is particularly reactive with water vapour due to its high Mg content [18, 19, 20, 21] and there is clear evidence of corrosion and oxidation of the Mg_2Si particles at the initiation sites (e.g. Figure 8). The greater reactivity of Mg_2Si will therefore help promote more rapid and greater hydrogen generation, which could in principle accelerate incubation by more effectively infusing the nearby grain boundaries and encouraging the first cracking event near the initiating features.

Overall, there will therefore be greater number and more reactive potential initiation sites per unit area in AA7449 than in AA7085. This could partly explain why there was, on average, a more rapid transition to long crack growth behaviour in AA7449 compared to in AA7085, despite the two alloys having similar incubation times (discussed further below). For example, a greater population of microstructural features offering suitable initiation sites will make the probability of finding an ideal initiation and short crack location more likely in AA7449.

The specific microstructure (e.g. intersecting grain boundaries) surrounding the initiation site is also important for the development of proto-cracks. Due to the larger rolling reduction, AA7449 exhibited a slightly greater grain aspect ratio than the AA7085 5:1 vs. 4.5:1 (L/ST), such that once a crack starts propagating in AA7449 there are slightly fewer potential obstacles like grain intersections per unit area, to impede initial crack growth [23]. More importantly, the different bulk alloy compositions and response to quenching means the two alloys have a large difference in their distributions and compositions of η GBPs. GB η precipitates are particularly important in sustaining cracking as their high Mg content provides a highly reactive proportion of the fracture surfaces for continued H generation. It has also recently been shown by DFT studies that the η - matrix interface is more susceptible to decohesion from H segregation than the Al-GBs themselves [55]. For these plate products, due to its higher quench sensitivity and higher equilibrium η volume fraction, AA7449 has a much higher overall area fraction of GBPs compared to AA7085 (52% vs 18% measured by applying the method outlined in Ref. [11]), although the Q-GBP's in AA7449 are slightly richer in Zn and Cu than in AA7085 [11]. AA7449 also displays a greater area fraction of smaller A-GBPs, but these age-induced more reactive precipitates have a similar composition in both alloys, due to their similar precipitation temperatures determined by their respective ageing treatments [56]. Overall, therefore, due to the higher area fraction of GBP's we expect a greater chemical reactivity of the GBs of AA7449, which will be more effective at providing a continuous source of hydrogen, and in addition the higher area coverage of GBP's will also reduce the mechanical strength of the boundaries and encourage hydrogen enhanced decohesion of a greater proportion the GB plane which is covered by matrix-precipitate interfaces.

Microstructural origin of initiating features

Initiation was found to occur exclusively within surface breaking, or very near surface, pore clusters which were usually associated with constituent particle aggregates. A low, 0.009%, volume fraction of very small gas pores (average diameter of 2.87 µm) was measured in the AA7085 thick plate using a novel femtosecond laser 3D serial sectioning technique (Fig. 13). The majority of these pores were found in clusters co-located with constituent particle aggregates (Figs. 4, 8 and 9). The pore clusters that led to primary and dominant cracks were all found to be located on grain boundaries. The co-location of constituent particles and gas pores with grain boundaries is to be expected in DC cast hot-rolled thick plates, as during solidification the hydrogen dissolved in the liquid concentrates in the last liquid to solidify in the inter-dendritic channels, which itself is enriched in solute [57]. H_2 remains supersaturated in these regions, which are subjected to a pressure gradient due to liquid feeding, and gas bubbles nucleate in the inter-dendritic liquid on re-entrant surfaces generated by first constituent particles to form, which are typically Fe rich phases like Al_7Cu_2Fe that will also trap them to become frozen within the dendrite and grain boundaries [50]. The pores that survive closure during rolling therefore tend to be found on HAGBs with constituent particle clusters unless substantial recrystallization has occurred, which was not the case for these materials [11, 40]. Commercial aerospace thick plates are subjected to hot rolling reductions of only 50-75% and this level of plane strain compression aligns the pores and constituent particles in the rolling plane, but is clearly not sufficient to fully heal all the gas pores. Compressed gas pores will contain a high pressure, and the H_2

must be removed by diffusion, typically along dislocation pipes to external surfaces during hot rolling, which is more difficult in thick plates. Thus, Although the pores become compressed and partially healed during hot rolling [58, 59] they will re-grow and spherodise during subsequent solution treatment [50]. High resolution XCT analysis by Toda et al. show that the porosity is not generally fully eliminated by rolling and that the resulting size range of the pores after solution treatment is in the few micron regime, in agreement with our observations [59, 60]. H_2 gas trapped within these pores is not expected to have any impact on the EIC process which relies on chemical charging by dissociated H^+ ions and any H_2 gas will be released in any event when the pores are sectioned to allow the environment to enter. Rolling may further be responsible for creating damage in constituent particle clusters which is again not necessarily fully healed by intrusion of the matrix at these moderate rolling reductions (e.g. Figs. 8, 9), which will create prior micro-fissures that can be exposed on sample preparation and after initial loading [61].

The prior surface condition of the samples is also very important in any corrosion/exposure test. Here, the 4PB tests were performed on carefully polished samples The sample preparation route employed used a water-free colloidal silica finish to produce a chemically un-etched surface that reduced the near-surface deformed layer to an absolute minimum (<100 nm). As such, it is recognised that the initiation sites seen in these tests may be different in manufactured components, where local sites of deep surface damage from machining may dominate over, or coincide, with heterogeneities such as the gas pores already present on the material. Materials produced for service applications would display a variety of different surface finishes, some cut edges and drilled holes can expose bare metal but this would both be covered in a near surface deformed layer. A near surface deformed layer can be beneficial and provide a barrier to the underlying susceptible microstructure or it can be highly active and susceptible to corrosion potentially promoting EIC initiation [62,, 63, 64, 65]. Most surfaces are subjected to a whole series of procedures so that they can be effectively painted, whilst much machining 'damage' may be removed often a thick anodised layer will be introduced. However even this protection cannot eliminate the initiation and growth of EIC [66]. Here, the pores themselves were often seen to be partially covered by a thin aluminium layer that was smeared over the surface during sample polishing, forming a partially enclosed environment. In only a very few cases was any evidence of contamination from the final polishing stages seen, which suggests that air bubbles trapped in these locations and the 'smeared cover' prevented them filling with liquid during polishing. The size of the pores and pore clusters in these materials, 2-10 µm, would mean that a rather substantial nanocrystalline near surface deformed layer would be necessary conceal them e.g. [67] although other influences such as the residual stresses at the surface which penetrate much deeper could also affect the initiation.

Stage 1: Incubation

During incubation changes take place in the sample following the loading of the specimens and exposure to the elevated temperature (70 °C) and humidity. In the experiments, the samples were first loaded, then heated, and then exposed to humidity. Modelling has shown that very high stresses are expected in ligaments separating a subsurface pore and a surface, which can easily exceed the yield stress when the ligament is less than one pore diameter thick [68, 69, 70]. X-ray CT studies have also shown that large constituent particles, close to, or at the surface can crack or de-bond during loading without any action from the environment [71](as can be seen in Fig. 7) although this can be enhanced with H-charging [54, 72]. On loading, the aluminium ligaments separating the pores, or separating pores from constituent particle aggregates, will become the focus of very high stress concentrations. The high levels of stress in the pore ligaments experienced during loading could easily lead to the ligaments breaking with an intergranular ductile-mechanism, possibly over a short duration associated with creep, which will be accelerated by heating to the test temperature, and this can also

encourage damage to the constituent particles by load shedding to these harder and stiffer phases. Creep deformation taking place will also be localised to the grain boundaries, probably within precipitate free zones [73]. In addition, any pre-existing damage to the constituent particles will open up and pre-existing sharp cracks may extend during loading.

In the subsequent introduction of the humidity a combination of such precursor damage features with continued creep and the presence of a reactive environment can thus readily lead to the conditions required for a proto-crack to develop. At the same time, it seems that the presence of a small fissure is a prerequisite for water condensation as there is no evidence suggesting the pores themselves filled with water. The sharp radius and the tight nature of these features will create preferential sites for water condensation [27, 74]. However, the process to condense liquid water from the vapour phase exterior environment is time-dependent and can take several hours at 50% RH [75, 76]. While, with sufficient humidity, on a flat surface islands of water form quickly to build up a continuous thin ~2 nm water of a few molecules thick it is known that more time is needed to create the more substantial volumes needed to fill surface penetrating fissures [4, 77, 78]. Within these fissures, liquid water, albeit at the microscale, can support increasingly aggressive corrosion reactions especially as the liquid incorporates ion species such as carbonate and bicarbonate ions originating from CO_2 in the atmosphere, and reacting with magnesium to form carbonate phases [79]. The presence of reactive constituent particles like Mg_2Si in AA7449, and the exposed Mg-rich chemically active η-phase particles, that precipitated on the pores and grain boundary surfaces during quenching (Fig. 8-10), provide the most preferential type of initiation site. Our observations (e.g. Fig. 4) further reveal the initiation sites of primary cracks were primarily of this type. This is probably due to the fact that these phases can greatly increase the rate and volume of generated H and may also assist in H entry as they do not form a barrier layer to hydrogen ingress as effective as Al_2O_3 over the Al matrix [80]. The incubation time for proto-crack formation may also be controlled partially by the rate pure water condenses from distilled water vapour, which first results in a relatively benign environment such that reactions with the metal are initially quite slow, but also by the time the confined environment of a fissure takes to create a more aggressive local environment to promote pre-cursor formation through incorporation of reactant ions. The evidence of carbon decoration on the η phase precipitates suggests that this is likely supplied by dissolution of CO_2 into the water forming carbonate and bi-carbonate ions (CO_3^{2-} & HCO_3^-respectively). This evidence can be combined with our observation of Cu nanoparticles which are produced through the reaction of Cu in carbonate and bicarbonate solutions leading to the creation of soluble Cu during Cu oxidation reactions [81]. It should, however, be noted that in contrast to SCC in immersed environments where extensive surface corrosion can take place the initiation sites seen in these alloys exposed in humid air were very small (<10 µm) and only lightly corroded across the fracture surface the surface oxide layer was much thinner < 20 nm thick over the Al matrix.

Interestingly, from the data presented in Fig. 2, no significant difference was seen between the incubation times for AA7449 and AA7085 (58.70 and 56.98 hours respectively), despite the higher densities of constituent particles and the inclusion of more reactive Mg_2Si particles in AA7449. This could suggest that incubation occurred at a similar rate for both alloys because it is dominated by a material-independent process (at least between alloys with similar chemistry). This could be related to the time necessary to condense sufficient water in surface fissures and develop the liquid chemistry required to support the corrosion reactions to hydrogen charge the stress concentrated regions and start the initiation process. However, further work is needed to investigate the role of time dependent condensation from other influences on the incubation time, such as creep damage, to test this hypothesis.

Stage 2: Pre-cursor: creation of a feature and transition to a GB to enable H-EIC

In some cases the pre-cursor stage is often significant as it describes a corrosion process (e.g. pitting) which maybe be a necessary pre-cursor to cracking [82]. However, these experiments showed only a minute level of localised corrosion damage, which was largely via dissolution of the surface exposed η phase precipitates, and also Mg_2Si in AA7449, which occurred before the proto-crack stage of EIC commenced. In these experiments the corrosion observed may assist penetration along a grain boundary, but the high local stress is clearly very important for mechanical separation of the grain boundary and this first penetration by an embryo crack along a grain boundary is most probably a stress-assisted corrosion process creating a high local stress intensity factor K.

At the initiation regions for cracking along the grain boundaries, which occurred at several orders of magnitude lower growth rates (Fig. 1b) the presence of condensed water was confirmed through the evidence of complete dissolution of the GB η-phase particles, although these regions were extremely small in extent reaching only 5-10 µm in radius. It is currently difficult to say whether this process took place through initial fracture of the grain boundary and subsequent corrosion, or this penetration was made through a coupled-damage and corrosion process, either way it's appearance was distinct from the subsequent brittle intergranular cracking. Corrosion forming pre-cursor features will produce hydrogen that will be absorbed locally and concentrate preferentially on the locally stressed GBs adjacent to the incubation site. Whether there is sufficient hydrogen charging to cause decohesion at this early stage is hard to determine, but the appearance of local plasticity on the fracture surfaces on the minute lightly corroded region before CAM's started to appear, suggests mechanical damage by creep-rupture combined with corrosion is first required to expose fresh grain boundary surface.

Stage 3. Proto-cracks

Proto-cracks form when the required ingredients to initiate an intergranular (IG) hydrogen-induced crack have been created and focussed at a specific location. Precursors are required to create the conditions for brittle IG cracks to first form; i.e. a sharp feature with a high stress concentration along a GB pathway infused with hydrogen. When the metastable hydrogen concentration locally exceeds a critical threshold for cracking [22] (i.e. the requirements are met), the process changes from a sharp feature to a hydrogen EIC crack which, given the extremely brittle appearance of the GB fracture surfaces, most probably occurs by a HEDE mechanism, as has been also suggested by other authors to be the dominant mechanism in similar Al-alloys [5, 6, 7, 12, 13, 14]. It should be noted that recent DFT simulations have demonstrated that HEDE can probably occur more readily by fracture of the interface between η phase precipitates with the Al matrix than by the grain boundaries themselves [55], but the GBs also rapidly lose their cohesive strength with increasing local hydrogen concentrations. There also appears to be no limit to the concentration of hydrogen that can segregate to a GB, or the η interface, which with sufficient hydrogen present can drastically reduce the cohesive strength [25]. It is therefore noteworthy that the area fraction of GB η precipitates in these alloys (in the T7651 temper) is extremely high and has been measured to be ~ 18% and 52% for AA7085 and AA7449 respectively.

CAM's were observed in both alloys extending up to ~50 µm from the initiation site and we suggest they define the extent of the proto-crack stage, which is the first stage of EIC and characterised by a slow moving crack that is intermittently arresting. The CAM's observed showed evidence of a locally thicker oxide up to a maximum of ~38 nm thick (with an average of 26 nm) (see Fig. 10). These bands of thicker-oxide also contained a distribution of Cu-nanoparticles ~10 nm in size, as well as a higher density of nano-pits formed by dissolution of the small η A-GBPs and possibly local attack of the matrix itself along the CAM lines. Greater Mg, and also Zn, were incorporated into the oxide along the CAM lines, dispersed from their original source in the η precipitates. It thus seems that the crack tip is still

sufficiently wet in this region to cause more aggressive chemical reaction and disperse the Mg and Zn, as well as precipitate Cu-nanoparticles, but the conditions for ionic transport were marginal as the oxide thickness was still influenced locally by the proximity to reacted η particles. In addition, the lack of an obvious 'trench' along the CAM bands and the fact that the CAM's appear more like miniature beach marks rather than a topographical feature formed by a ductile PFZ, suggests no significant corrosive attack of the Al matrix took place or ductile blunting of the crack tip following a burst of rapid brittle fracture. Overall, this behaviour is thus consistent with the presence of a very small and thin water meniscus and the crack advancing in small steps of brittle H-decohesion, followed by a static phase where more corrosion was required to re-charge the crack tip hydrogen concentration above a critical threshold level.

It is also evident that to develop a viable initiation site the microstructural features developed in the incubation and precursor stages must connect effectively to a grain boundary. This requirement explains why there can be so many surface-connected constituent particles, pores, or fissures, and yet so few EIC cracks. For example, if the connected grain boundary is unfavourably oriented (with respect to the applied stress) or is tortuous, or disrupted in some way, proto-cracks either cannot form or can propagate only a short distance before arresting.

Stage 4: Short crack regime

Beyond the ~50 µm regions of CAMs surrounding the initiation site there is still a notable period of slow crack growth in the measured data in Figure 1, where the cracks are 'short' relative to the grain size, but CAM's are no longer observed on the fracture surfaces; i.e. from between ~50 µm up to the transition crack length. We have defined this stage as occurring from after the proto-cracks form until they accelerate to make the transition to a 'long crack' behaviour, where the crack growth rate becomes more consistent and of higher velocity.

It was noted in Fig. 2 that there was a large variability in the crack lengths when they made their transition to more rapidly growing 'long' cracks. The erratic velocity, and intermittent arresting of the cracks as well as the wide range of crack lengths observed before their transition to long cracks, is due to the local microstructure surrounding the different initiation sites. Some proto-cracks will find themselves on a geometrically favourable crack path following nucleation; i.e. a single uninterrupted planar high grain boundary oriented perpendicular to the applied stress. In other cases, grain intersections, changes of direction, intervening IMC particle clusters, unfavourable local chemistry or a lower rate of hydrogen concentration etc., can act as obstacles causing the cracks to slow down and temporarily arrest. Events such as crack blunting, change of direction and crack branching can all have this effect. In these alloys the transition from short cracks to long cracks occurred within the range of 180-3300 µm and averaging around 800 µm corresponding closely to ~1 grain length in the L direction in these materials (~600 µm). Whilst no discernible difference was seen between the two alloys regarding their incubation time a significant difference was seen in the transition crack length, which was 0.38 mm for AA7449 and 1.61 mm for AA7085, despite the two materials having similar grain sizes. In both cases there was over an order of magnitude spread in the transition crack lengths. It can be seen from Fig. 2 that six out of nine cracks in AA7449 transitioned at < 300 µm, but for AA7085 five out of seven cracks transitioned at the greater length of > 500 µm, making this aspect of their different behaviour pronounced. From our analytical calculations a length of 420 µm, assuming a semi-elliptical crack with c/a ratio of 1.5 corresponds to a K of 6 MPa√m. This corresponds quite closely to the threshold K_{IEIC} for these alloys determined from long crack growth studies in DCB experiments [40]. But, for example, AA7085 has some cracks transitioning to a long crack behaviour at 300 µm where the K can be estimated to be ~ 5 MPa√m and others at a length of 3.29 mm where K would be estimated to be ~15 MPa√m. This large variation can only be explained by the role of the local

microstructure, which is controlling the local path and shape of the crack and therefore the effective local K and the resistance offered by the material. The difference between the two alloys also suggests that the boundaries in AA7449 are intrinsically less resistant to sustained crack propagation than in AA7085, probably because of the higher area fraction of GB η precipitates in this alloy.

The fracture surface in the transition region, 200-500 µm away from the proto-crack (CAM) region, shows a relatively thin (~5 nm) oxide of uniform thickness across the Al matrix and a thicker (~15 nm) oxide on the η-phase GBPs. The oxide covering the η-phase particles incorporates Mg and Zn, but these elements remain localised to the GBPs and were not dispersed away from the GBPs. While the Mg appeared uniform the Zn seemed to show some clustering from the STEM-EDX observations. These oxide features were the same as observed on the fracture surfaces of the long cracks. Overall, this suggests a very limited presence of liquid water in cracks that are starting to propagate at a much higher rate in the long crack regime (i.e. there is an extremely localised nm-scale crack tip meniscus). The fact that the oxidation of the fracture surface away from the CAM's shows the same degree of oxidation observed from exposing an intergranular fracture surface (without a crack tip environment) to the same high humidity higher temperature environment (see Table 3), implies that once the crack grows beyond a certain length and the rate accelerates to a level that is not seen in lower Zn containing alloys like AA7050 (i.e. 10x higher) there is no evidence of corrosion that requires liquid water taking place at the crack tip. It is interesting to note that there is some evidence that for high Zn-content alloys cracking can even occur in inert environments [4] but the requirements for initiation and propagation in this case are not clear.

Transition to Long cracks'

The transition to a 'long crack' behaviour essentially takes place when a crack (in 3D) reaches sufficient size to overcome local microstructural obstacles that in the short crack regime can severely impede more consistent and faster crack growth [30]. Although microstructural crack obstacles will still exist, when the crack size is sufficient, such that it is only locally affected at positions on the crack front, this will create a drag on the average growth velocity but have an overall smaller influence on the intermittent crack growth rate. This occurs when the effective K is sufficiently high and the supply and concentration of H across the crack front sufficiently reliable for the propagation not to be dominated by individual microstructural obstacles. In general, for the elliptical, or half-penny, shaped cracks in the 4PB test when it grows bigger the crack front also gets longer. As well as reducing the relative importance of individual obstacles, a larger crack will have more options to find an alternative path through the microstructure, which are not available to a smaller crack with lower driving force. On average the K value this is occurs at is the K_{IEIC} as measured from DCB test and the K required for a 'macroscale' crack to avoid arrest [40, 83]. However, given K is dependent on crack geometry, this implies the more rapid transition in crack growth rate with crack length seen in AA7449 is probably associated with a greater supply of hydrogen from the larger area of freshly exposed η precipitates on the GB plane in this alloy and the fact that these interfaces may be more susceptible to embrittlement. In addition, the reaction of the Mg_2Si at the initiation sites can effectively infuse the local microstructure with hydrogen to accelerate this transition.

Summary of the initiation process

Finally, Fig. 14 provides a summary of the sequence of initiation to long crack growth in new-gen high-Zn 7xxx alloys exposed to humid air observed in this work. A crucial role is played by gas pores in clusters, co-located with constituent particles, which are the preferred sites for initiation under these conditions. These sites create highly stressed intervening metal ligaments susceptible to rupture (Fig. 14a). The first penetration along a grain boundary creates a sharp feature, which is not yet a propagating EIC crack and is defined as a crack pre-cursor. This sharp feature will have a sufficiently

high stress concentration at it's tip, exists on a grain boundary and becomes filled with water condensed from the environment with sufficient time. This, with continued mechanical damage, creates a site of focussed chemical activity generating hydrogen which diffuses into the microstructure (Fig. 14b). With this condition established, hydrogen EIC cracking commences as proto-cracks when the local H concentration becomes sufficient for the boundary to decohere and separate under the locally high stresses (Fig. 14c). A steady state is then ultimately achieved whereby the hydrogen needed to embrittle the grain boundary ahead of the crack is generated at the crack tip at a sufficient rate, as new GB surface is exposed, combined with sufficient stress to cause grain boundary decohesion. As the crack grows and the stress intensity increases, and the local microstructure influence reduces, it starts to accelerate and after a period the cracks appear to grow at a high enough rate for there to be no longer any evidence for corrosion requiring a thick water layer taking place at the crack tip e.g. dissolution or precipitation. Instead, oxidation of the matrix and η-phase particles by a thin surface water layer generates sufficient hydrogen concentration on the GB ahead of the crack, such that in combination with the greater driving force from the sharper and longer crack it enters sustained long crack growth (Fig. 14d).

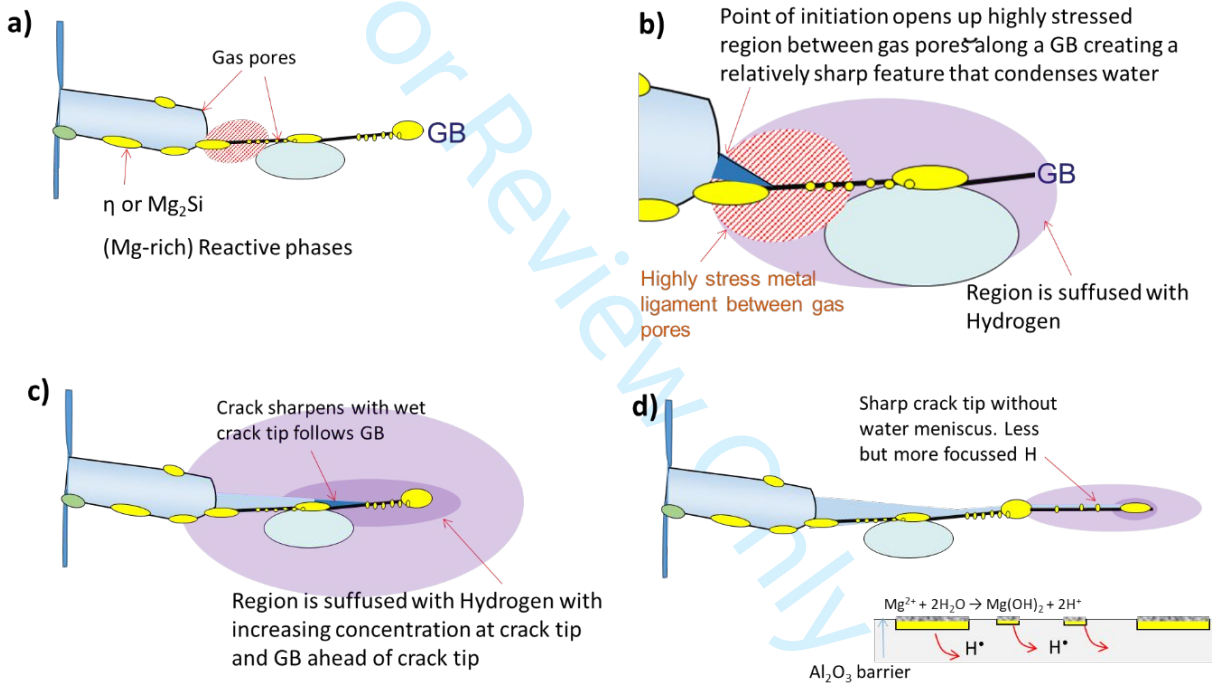

Figure 14. Schematic summary of the initiation process seen in new-gen high Zn alloys when exposed to humid air environments; a) surface breaking pore and metal ligament between sub-surface pore situated on a GB. Pore interior and GB are plated with η-phase. Ligament is highly stressed under load b) GB connected to metal ligament between pores is penetrated and the sharp fissure condenses water leading to corrosion in this region, hydrogen is evolved and suffuses surrounding metal c) EIC cracking of GB starts with a wet crack tip and crack sharpens focussing K and hydrogen at crack tip d) Cracking extends now without a wet tip, a sharp crack and oxidation of metal are finely focussed at crack tip leading to high local K and hydrogen. A combination of the metal and M-phase oxidation provide sufficient hydrogen for cracking under these high K conditions.

Conclusions

The EIC initiation and transition to long crack growth behaviour of two new generation high Zn 7xxx series alloys AA7085-T7651 and AA7449-T7651 have been compared in thick hot rolled plates, when exposed to warm humid air. Both alloys showed consistent results with a highly brittle EIC behaviour with very limited surface corrosion. Multiple initiation sites have been accurately identified and investigated in forensic detail. Precise detection of the initiation sites through the application of an in-

situ optical monitoring system gave confidence in identification of the correct sites for subsequent investigation, which were analysed using advanced electron microscopy techniques; including STEM-EDX, fs-laser-Xe^+ plasma FIB sectioning and high resolution low energy SEM-EDX. From this we conclude that:

- Surface connected gas pores, within pore clusters, combined with constituent particles and a reactive Mg-rich phase, connected to a stressed grain boundary, determine the preferred initiation site feature in both alloys.
- The precursor sites are nanoscale corrosion features that are exceptionally localised, less than 10 µm in area, with only a depth of <50 nm at the exposed surface and are created by metal ligaments separating neighbouring pores and/or constituent particles that become a focal point for initial rupture. This creates a fissure which condenses water and results in highly localised corrosion along a grain boundary generating H which is concentrated at the stress concentration.
- The incubation period is probably controlled by the time for condensation of sufficient water in such a feature and to establish a suitable precursor reaction centre, where mechanical damage by highly localised creep-rupture, combined with corrosion, is required to expose fresh surface and develop a high enough rate of local H-charging. Here, the incorporation of carbonate/bicarbonate ions may also be important for the reactions observed, originating from CO_2 in the atmosphere.
- Following H charging, by corrosion at precursor features, of a highly stressed, connected, grain boundary the conditions are established where an EIC proto-crack can first propagate by a hydrogen-enhanced decohesion mechanism.
- Proto-crack growth of short cracks is first slow and intermittent leading to a small region (<50 µm) surrounding the initiation sites leading to the formation of CAM's, but again only light surface corrosion was observed. Overall, this suggested the presence of a very small water meniscus and that, at this stage, the crack advances in small steps of brittle hydrogen enhanced decohesion followed by a static period where more corrosion was required to re-charge the crack-tip bringing the hydrogen concentration above a critical threshold level.
- Microstructurally short cracks then continued to propagate slowly and erratically, being very sensitive to microstructural obstacles, but without CAM markings and the fracture surfaces no longer displayed the characteristics of a wet crack tip. The transition to a 'long crack' occurred once the estimated K reached a similar value to K_{IEIC} (6-7 MPa √m) measured in long crack DCB tests and lead to a high, less erratic, crack growth velocity, which is ~ ten times faster than that seen in lower Zn alloy like AA7050 in a similar T7 temper condition.
- The 'long crack' behaviour was defined as the point when the cracks transitioned to a more consistent maximum velocity and the short to long transition was observed to take place at a wide range, 180 to 3000 µm, of crack lengths.
- Cracking in the short and long crack regime showed minimal surface reaction, with only a very thin layer of surface oxidation, suggesting at these high crack growth rates there is insufficient water for electrochemical corrosion i.e. no dissolution, precipitation or micron-scale transport of ions, meaning that little total hydrogen was necessary for cracking, but sufficient hydrogen must still be both generated and become concentrated locally at the crack tip.
- The results further show that the proto-crack and short crack stages are critical for overall performance and time to failure for these alloys and could account for the different initiation times seen between AA7449 and AA7085, as well as the fact that despite the presence of an abundance of potential initiation sites in both materials only a few were able to effectively transition from proto-crack sites to form sustainable long cracks.

Acknowledgements

We are grateful to the Royal Academy of Engineering, UK, and Airbus for financial support through the Airbus-University of Manchester Centre for Metallurgical Excellence. The authors are also appreciative of the EPSRC programme grant LightForm (EP/R001715/1) and the Metallic Systems CDT (EP/L016273/1), and the Henry Royce Institute for Advanced Materials, funded through EPSRC grants EP/R00661X/1, EP/S019367/1, EP/P025021/1 and EP/P025498/1 for supporting aspects of this research.

References

1. H Brown, Aluminum and its Applications, 1948, Pitman Publishing Corporation, New York

2. Schwarzenböck E, Wiehler L, Heidenblut T, Hack T, Engel C, Maier HJ. Crack initiation of an industrial 7XXX aluminum alloy in humid air analyzed via slow strain rate testing and constant displacement testing. Mater Sci Eng A. 2021 Feb 15;804:140776.

3. A. Poznak, D, Freiberg, P. Sanders, In: Fundamentals of Aluminium Metallurgy – Recent Advances : Chapter 10 - Automotive Wrought Aluminium Alloys, Woodhead Publishing Series in Metals and Surface Engineering 2018, Pages 333-386 https://doi.org/10.1016/B978-0-08-102063-0.00010-2

4. N.J. H. Holroyd, T. L. Burnett, J. J. Lewandowski and G. M. Scamans, Environment-Induced Cracking of High-Strength Al-Zn-Mg-Cu Aluminum Alloys - Past, Present and Future, Corrosion 79 (2023) pp. 48-71

5. N J H Holroyd, G M Scamans, Crack Propagation during Sustained-Load Cracking of Al-Zn-Mg-Cu alloys exposed to Moist Air of Distilled Water, *Metall. Mater. Trans A* 42A, (2011): p. 3979-3998.

6. N J H Holroyd, G M Scamans, Stress Corrosion Cracking in Al-Zn-Mg-Cu Alloys in Saline Environments, *Metall. Mater. Trans A* 44A, (2013): p. 1230-1253.

7. De Francisco U, Larrosa NO, Peel MJ. Hydrogen environmentally assisted cracking during static loading of AA7075 and AA7449. Mater Sci Eng A. 2020 Jan 20;772:138662.

8. EASA, Environmentally Assisted Cracking in Certain Aluminum Alloys, European Aviation Safety Information Bulletin 2018-04RI, 2018. https://ad.easa.eurpoa.eu/ad/2018-04R1

9. Y Aboura, A J Garner, R Euesden, Z Barrett, C Engel, N J H Holroyd, P B Prangnell, T L Burnett, Understanding the environmentally assisted cracking (EAC) initiation and propagation of new generation 7xxx alloys using slow strain rate testing, *Corrosion Science* 199 (2022): 110161.

10. N J H Holroyd, "Environment-Induced Cracking of High-Strength Aluminum Alloys", In *Environment-Induced Cracking of Metals* (Houston, TX: National association of Corrosion Engineers, 1989), p. 311- 345.

11. Garner A, Euesden R, Yao Y, Aboura Y, Zhao H, Donoghue J, et al. Multiscale analysis of grain boundary microstructure in high strength 7xxx Al alloys. Acta Mater. 2021 Jan 1; 202: 190–210.

12. S. P. Lynch, Hydrogen embrittlement phenomena and mechanisms, Corros Rev 30 (2012): 105–123

13. R.G. Song, W. Dietzel, B.J. Zhang, W.J. Liu, M.K. Tseng, A. Atrens, Stress corrosion cracking and hydrogen embrittlement of an Al–Zn–Mg–Cu alloy, Acta Materialia, Volume 52, Issue 16, 20 September 2004, Pages 4727-4743

14. Hang Su, Hiroyuki Toda, Kazuyuki Shimizu, Kentaro Uesugi, Akihisa Takeuchi, Yoshio Watanabe, Assessment of hydrogen embrittlement via image-based techniques in Al–Zn–Mg–Cu aluminum alloys, Acta Materialia, Volume 176, 1 September 2019, Pages 96-108

15. Ian M. Robertson, P. Sofronis, A. Nagao, M. L. Martin, S. Wang, D. W. Gross & K. E. Nygren, Hydrogen Embrittlement Understood, Metallurgical and Materials Transactions A volume 46, pages2323–2341 (2015)

16. Huan Zhao, Poulami Chakraborty, Dirk Ponge, Tilmann Hickel, Binhan Sun, Chun-Hung Wu, Baptiste Gault, Dierk Raabe, Hydrogen trapping and embrittlement in high-strength Al alloys, Nature (2022) Volume 602, Issue 7897, Pages 437-441

17. R N Parkins, Stress Corrosion Spectrum, British Corrosion Journal 7, (1972) 15-28.

18. Mingyang Chen Xu Zheng Kezhun He Shengdan Liu Yong Zhang, Local corrosion mechanism of an Al-Zn-Mg-Cu alloy in oxygenated chloride solution: Cathode activity of quenching-induced η precipitates Corrosion Science Volume 191, October 2021, 109743

19. Birbilis, N. & Buchheit, R. G. Electrochemical Characteristics of Intermetallic Phases in Aluminum Alloys: An Experimental Survey and Discussion. J. Electrochem. Soc. 152, B140 (2005)

20. Mingyang Chen, Xu Zheng, Kezhun He, Shengdan Liu, Yong Zhang, Local corrosion mechanism of an Al-Zn-Mg-Cu alloy in oxygenated chloride solution: Cathode activity of quenching-induced η precipitates, Corrosion Science, Volume 191, October 2021, 109743

21. S.P. Knight, N. Birbilis, B.C. Muddle, A.R. Trueman, S.P. Lynch, Correlations between intergranular stress corrosion cracking, grain-boundary microchemistry, and grain-boundary electrochemistry for Al–Zn–Mg–Cu alloys, Corrosion Science, Volume 52, Issue 12, December 2010, Pages 4073-4080

22. G M Scamans, C D S Tuck, The role of hydrogen in environmentally sensitive mechanical behaviour in AlZnMg alloys, in Mechanisms of environment sensitive cracking of materials, Proceedings of an International conference organised by the Metals Society, University of Surrey, Guildford, 1977

23. T Warner; D Koschel; R Whelchel; P Smith; G Scamans; R Merrill Corrosion, 79 (2022) 4142

24. Young GA, Scully JR. The effects of test temperature, temper, and alloyed copper on the hydrogen-controlled crack growth rate of an Al-Zn-Mg-(Cu) alloy. Metall Mater Trans A. 2002 Apr 1;33(4):1167–81.

25. Benjamin T Wilson, Joseph D Robson, Pratheek Shanthraj, Christopher P Race, Simulating intergranular hydrogen enhanced decohesion in aluminium using density functional theory 2022/2/17, Modelling and Simulation in Materials Science and Engineering, Volume 30, Issue 3, Pages 035009.

26. Tomohito Tsuru, Kazuyuki Shimizu, Masatake Yamaguchi, Mitsuhiro Itakura, Kenichi Ebihara, Artenis Bendo, Kenji Matsuda & Hiroyuki Toda, Hydrogen-accelerated spontaneous microcracking in high-strength aluminium alloys, Scientific Reports volume 10, Article number: 1998 (2020)

27. S. P. Knight Stress corrosion cracking of Al-Zn-Mg-Cu alloys : effects of heat-treatment, environment, and alloy composition, Thesis (2008) Monash

28. R.H. Jones, Stress-Corrosion Cracking. Materials Performance and Evaluation, Second ed, ASM International (1992) IBSN 0-87170-441-2

29. R.W. Staehle, Quantitative micro-nano (QMN) approach to SCC mechanism and prediction-starting a third meeting, Proc. 15th Int. Conf. Environ. Degrad. Mater. Nucl. Power Syst. — Water React. John Wiley & Sons, Inc., 2017, pp. 1535–1629

30. V C Gudla, M Storm, B C Palmer, J J Lewandowski, P J Withers, N J H Holroyd, T L Burnett, Environmentally Induced Crack (EIC) initiation, Propagation, and Failure: A 3D in-situ time-lapse study of AA5083-H131, Corrosion Science, 2020: 174, 108834.

31. R J H Wanhill, Short Stress Corrosion Cracks in Aluminium Alloy Components, Materials & Design, Volume 7, Issue 5, September–October 1986, Pages 256-261

32. NJ Henry Holroyd, TL Burnett, M Seifi, JJ Lewandowski, Improved understanding of environment-induced cracking (EIC) of sensitized 5XXX series aluminium alloys, Materials Science and Engineering: A (2017) Volume 682, Pages 613-621

33. A. Turnbull Modeling of the Chemistry and Electrochemistry in Cracks—A Review, Corrosion, 57 (2001) p. 175-187

34. T. H. Nguyen; B. F. Brown; R. T. Foley, On the Nature of the Occluded Cell in the Stress Corrosion Cracking of AA 7075-T651—Effect of Potential, Composition, Morphology, Corrosion, 38 (1982), pp. 319–326.

35. KR Cooper, RG Kelly, Crack tip chemistry and electrochemistry of environmental cracks in AA 7050, Corrosion Science 49 (6), 2636-2662

36. R P Gangloff, Hydrogen Assisted Cracking of High Strength Alloys, 2003, Book Comprehensive Structural Integrity, Volume 6, Pages, 31-101, Publisher Elsevier

37. Christine Blanc; Roland Oltra, Environment-Assisted Crack Initiation in Aluminum Alloys Studied by Local Probe Techniques, Corrosion (2023) 79, pp. 17–34

38. R. J. Gest; A. R. Troiano, Stress Corrosion and Hydrogen Embrittlement in an Aluminum Alloy, Corrosion, 30 (1974), pp. 274–279.

39. Emilio Martínez-Pañeda, Christian F Niordson, Richard P Gangloff, Strain gradient plasticity-based modeling of hydrogen environment assisted cracking Acta Materialia, Volume 117, (2016) Pages 321-332

40. Elisabeth Schwarzenböck, Eric Ollivier, Alistair Garner, Alex Cassell, Theo Hack, Zak Barrett, Christian Engel, Tim L Burnett, NJ Henry Holroyd, Joseph D Robson, Phil B Prangnell, Environmental cracking performance of new generation thick plate 7000-T7x series alloys in humid air, 2020, Corrosion Science, Volume 171, Pages 108701

41. X. Xu, M. Hao, J. Chen, W. He, G. Li, K. Li, C. Jiao, X.L. Zhong, K.L. Moore, T.L. Burnett, X. Zhou, Role of constituent intermetallic phases and precipitates in initiation and propagation of intergranular corrosion of an Al-Li-Cu-Mg alloy, Corrosion Science, Volume 201, June 2022, 110294

42. R T Euesden et al, In-Situ Observation of Environmentally Assisted Crack Initiation and Short Crack Behaviour of New-Generation 7xxx Series Aluminum Alloys in Humid Air, Accepted to Corrosion Science.

43. Sutton, M. A., Wolters, W. J., Peters, W. H., Ranson, W. F., & McNeill, S. R. (1983). Determination of displacements using an improved digital correlation method. *Image and vision computing*, 1(3), 133-139.

44. Lucas, B. D., & Kanade, T. An iterative image registration technique with an application to stereo vision. IJCAI'81: Proceedings of the 7th international joint conference on Artificial intelligence - Volume 2, August 1981 Pages 674–679

45. A W Thompson, Z D Harris, J T Burns, Examination of focused ion beam-induced damage during platinum deposition in the near-surface region of an aerospace aluminum alloy, (2019), Micron, Volume 118, Pages 43-49

46. A Garner, J Donoghue, R Geurts, Y Al Aboura, B Winiarski, P B Prangnell, T L Burnett, Large-scale serial sectioning of environmentally assisted cracks in 7xxx Al alloys using femtosecond laser-PFIB, (2022) Materials Characterization, Volume 188, Pages 111890

47. K. J. Miller, THE SHORT CRACK PROBLEM, Fatigue & Fracture of Engineering Materials & Structures, Volume5, Issue3, July 1982, Pages 223-232

48. A Turnbull, Reflections on Early Stages of Environmentally Assisted Cracking from Corrosion Pits, Corros. Mater. Degrad. 2021, 2(4), 568-581

49. D Najjar, T Magnin, T.J Warner, Influence of critical surface defects and localized competition between anodic dissolution and hydrogen effects during stress corrosion cracking of a 7050 aluminium alloy, Materials Science and Engineering: A, Volume 238, Issue 2, 15 November 1997, Pages 293-302

50. H. Toda T. Hidaka, M. Kobayashi, K. Uesugi, A. Takeuchi, K. Horikawa, Growth behavior of hydrogen micropores in aluminum alloys during high-temperature exposure Acta Materialia 57 (2009) 2277–2290

51. G M Scamans, Discontinuous propagation of stress corrosion cracks in Al-Zn-Mg alloys, Scripta Metallurgica, Volume 13, Issue 4, April 1979, Pages 245-250

52. S P Lynch, Progression markings, striations, and crack-arrest markings on fracture surfaces. Mater Sci Eng A. 2007 Nov 15;468–470:74–80.

53. J.C. Newman, I.S. Raju, An empirical stress-intensity factor equation for the surface crack, Eng. Fract. Mech. 15 (1981) 185–192. https://doi.org/10.1016/0013-7944(81)90116-8.

54. U. De Francisco, F. Beckmann, J. Moosmann, N. O. Larrosa, M. J. Peel, 3D characterisation of hydrogen environmentally assisted cracking during static loading of AA7449-T7651, International Journal of Fracture volume 232, pages93–116 (2021)

55. Talk given at The International Conference on Aluminum Alloys ICAA 18 2022, Toyama O11-5-2 Invited: Hydrogen trapping energy at the incoherent interface in aluminum alloys: first-principles calculations, Masatake YAMAGUCHI, Japan Atomic Energy Agency (Japan)

56. Yichao Yao, PhD Thesis, Phase field model on grain boundary microstructures in 7xxx aluminium alloys, The University of Manchester, 2023

57. Devletian and Wood, Factors affecting porosity in aluminium welds-a review, ISSN 0043-2326, Welding Research Council, 1983 pp 1-18

58. Yongfu Wu, Huixue Jiang, Chun Zou, Kangcai Yu,Hiromi Nagaumi, Numerical Simulation of Pore Evolution of 7050 Aluminum Alloy during Hot Compression Process, Materials Science Forum, ISSN: 1662-9752, Vol. 879, pp 2119-2124

59. H. Toda, K. Minami, K. Koyama, K. Ichitani, M. Kobayashi, K. Uesugi, Y. Suzuki, Acta Materialia 57 (2009) 4391–4403

60. E. Nizery, H. Proudhon, J.-Y. Buffiere, P. Cloetens, T. F. Morgeneyer, S. Forest, Three dimensional characterization of fatigue relevant intermetallic particles in high-strength aluminium alloys using synchrotron X-ray nanotomography, Philosophical Magazine, 95 (2015) 2731-2746

61. Y S K Yoo, Y Su, S Das, R Hamerton, J Kacher, Multiscale electron microscopy of grain boundary-mediated crack initiation in AA6451 during three-point loading, Mat. Sci. & Eng. A, 833 (2022) 142572

62. G. M. Scamans, M. F. Frolish, W. M. Rainforth, Z. Zhou, Y. Liu, X. Zhou, G. E. Thompson, The ubiquitous Beilby layer on aluminium surfaces, Surf. Interface Anal., 2010, 42, 175–179.

63. X Zhou, Y Liu, G E Thomson, G M Scamans, P Skelton, J A Hunter, Near-Surface Deformed Layers on Rolled Aluminum Alloys, Metall. and Material Transactions A, 2011, 42A, 1373-1385.

64. P J E Forsyth, Sequence of corrosion attack of machining induced flow zone produced on some Al alloys that leads to rapid intergranular penetration, Material Science and Technology, 1998, 14: 151-160.

65. Shan-Shan Wang, D. Huber, J.D. Poplawsky, H. Colijn, G.S. Frankel, The subsurface structure of abraded Al–Zn–Mg–Cu alloy, Materialia, 10.1016/j.mtla.2021.101065, 16, (101065), (2021).

66. S. Lynch, A review of underlying reasons for intergranular cracking for a variety of failure modes and materials and examples of case histories, Engineering Failure Analysis 100 (2019) 329–350

67. Winiarski, M. Benedetti, V. Fontanari, M. Allahkarami, J.C. Hanan, P.J. Withers, High Spatial Resolution Evaluation of Residual Stresses in Shot Peened Specimens Containing Sharp and Blunt Notches by Micro-hole Drilling, Micro-slot Cutting and Micro-X-ray Diffraction Methods Experimental Mechanics volume 56, pages1449–1463 (2016)

68. S Tammas-Williams, PJ Withers, I Todd, PB Prangnell, The influence of porosity on fatigue crack initiation in additively manufactured titanium components, Scientific reports 7 (1), 7308, 2017

69. A. Messager, A. Junet, T. Palin-Luc, J-Y. Buffiere, N. Saintier, N. Ranc, M. El May, Y. Gaillard, A. King, A. Bonnin, Y. Nadot, In situ synchrotron ultrasonic fatigue testing device for 3D characterisation of internal crack initiation and growth, Fatigue Fract Eng Mater Struct. 2020;43:558–567.

70. J-Y. Buffière, S. Savelli, P.H. Jouneau, E. Maire, R. Fougères, Experimental study of porosity and its relation to fatigue mechanisms of model Al–Si7–Mg0.3 cast Al alloys, Materials Science and Engineering: A, Volume 316, Issues 1–2, 15 November 2001, Pages 115-126

71. D. Naragani, M. D. Sangid, P. A. Shade, J. C. Schuren, H. Sharma, J-S. Park , P. Kenesei, J. V. Bernier, T. J. Turner, I. Parr, Investigation of fatigue crack initiation from a non-metallic inclusion via high energy x-ray diffraction microscopy, Acta Materialia, Volume 137, 15 September 2017, Pages 71-84

72. Y. Wang, H. Toda, Y. Xu, K. Shimizu, K. Hirayama, H. Fujihara, A. Takeuchi, M. Uesugi, In-situ 3D observation of hydrogen-assisted particle damage behavior in 7075 Al alloy by synchrotron X-ray tomography, Acta Materialia, Volume 227, 1 April 2022, 117658

73. M S Hunter, W G Fricke, Study of Crack Initiation Phenomena associated with Stress Corrosion of Aluminum Alloys – Final Report, NASA Contract NAS 8-20936, 1966.

74. L. R. Fisher, R. A. Gamble & J. Middlehurst, The Kelvin equation and the capillary condensation of water, Nature volume 290, pages575–576 (1981)

75. S. M. Weiderhorn Influence of Water Vapor on Crack Propagation in Soda-Lime Glass, J. Am. Ceram. Soc, Volume50, Issue8, August 1967, Pages 407-414

76. M. Ciccotti, M. George, V. Ranieri, L. Wondraczek, C. Marlière, Dynamic condensation of water at crack tips in fused silica glass, Journal of Non-Crystalline Solids, Volume 354, Issues 2–9, 15 January 2008, Pages 564-568

77. Hind A. Al-Abadleh and V. H. Grassian, FT-IR Study of Water Adsorption on Aluminum Oxide Surfaces, Langmuir 2003, 19, 2, 341–347

78. T. E. Graedel Corrosion Mechanisms for Aluminum Exposed to the Atmosphere J. Electrochem. Soc. (1989) 136 204C

79. L Whitby, The atmospheric corrosion of Magnesium, Trans. Faraday Soc., 1933,29, 844-853

80. Xie D Wang Z Sun J et al, In situ study of the initiation of hydrogen bubbles at the aluminium metal/oxide interface, Nature Materials, (2015), 899-903, 14(9)

81. M. Perez Sanchez, M . Barrera, S . Gonzalez, R. M . Souto, Electrochemical behaviour of copper in aqueous moderate alkaline media, containing sodium carbonate and bicarbonate and sodium perchlorate, Electrochimica Acta, Vol . 35, No . 9, pp . 1 33 7-1343, 1990

82. Turnbull A, Wright, L Crocker, New insight into the pit-to-crack transition from finite element analysis of the stress and strain distribution around a corrosion pit, Corrosion Science, (2010), 1492-1498, 52(4)

83. R J H Wanhill, Short stress corrosion cracks in aluminium alloy components, Materials & Design, Volume 7, Issue 5, September–October 1986, Pages 256-261

Supplementary information

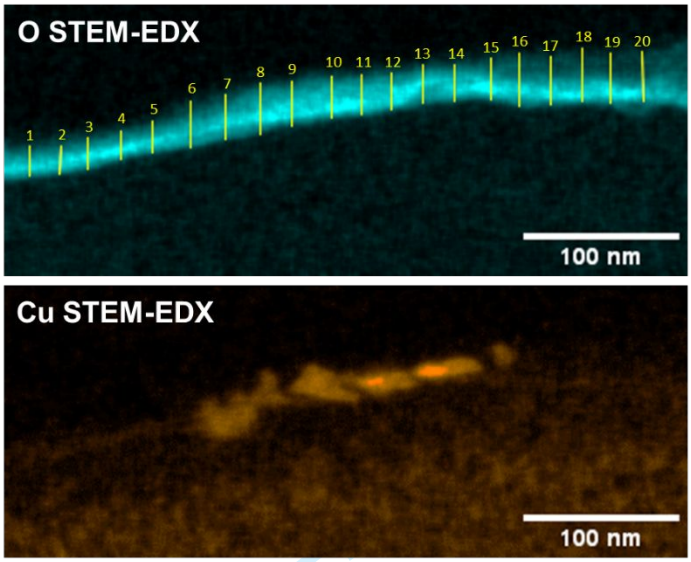

Line #	Length (nm)
1	19.86
2	18.80
3	20.92
4	18.80
5	20.92
6	29.79
7	29.09
8	32.62
9	28.02
10	26.60
11	25.53
12	23.40
13	24.12
14	24.11
15	27.30
16	34.04
17	30.50
18	34.40
19	31.92
20	31.74
Mean	26.62
SD	5.11
Min	18.80
Max	34.40

Figure S1. STEM-EDX spectrum maps of O and Cu showing the measurement of the oxide film thickness at a CAM line location

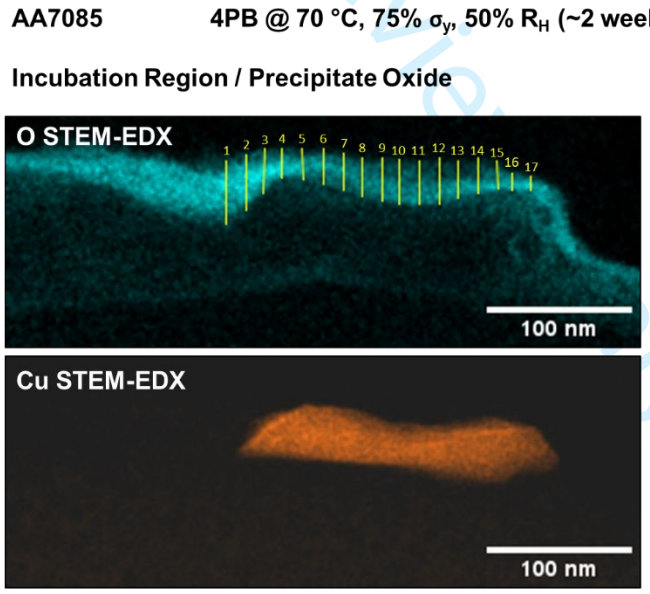

Line #	Length (nm)
1	42.91
2	38.65
3	30.50
4	20.21
5	20.92
6	24.47
7	25.89
8	27.30
9	29.43
10	30.85
11	30.14
12	31.91
13	24.83
14	24.82
15	19.51
16	12.06
17	10.29
Mean	26.16
SD	8.30
Min	10.29
Max	42.91

Figure S2. STEM-EDX spectrum maps of O and Cu showing the measurement of the oxide film thickness at an η phase precipitate >1 mm from the initiation site